creative commons

COMMONS DEED

저작자표시-비영리-변경금지 2.0 대한민국

이용자는 아래의 조건을 따르는 경우에 한하여 자유롭게

- 이 저작물을 복제, 배포, 전송, 전시, 공연 및 방송할 수 있습니다.

다음과 같은 조건을 따라야 합니다:

저작자표시. 귀하는 원저작자를 표시하여야 합니다.

비영리. 귀하는 이 저작물을 영리 목적으로 이용할 수 없습니다.

변경금지. 귀하는 이 저작물을 개작, 변형 또는 가공할 수 없습니다.

- 귀하는, 이 저작물의 재이용이나 배포의 경우, 이 저작물에 적용된 이용허락조건을 명확하게 나타내어야 합니다.
- 저작권자로부터 별도의 허가를 받으면 이러한 조건들은 적용되지 않습니다.

저작권법에 따른 이용자의 권리는 위의 내용에 의하여 영향을 받지 않습니다.

이것은 이용허락규약(Legal Code)을 이해하기 쉽게 요약한 것입니다.

Disclaimer

dCollection

이학박사 학위논문

Assessment of Fluid Flow and Solute Transport Characteristics through a Rough - Walled Fracture with Flow Imaging

유체 흐름 시각화 기법을 이용한 거친 단열 조건에서의 유체 유동 및 용질 거동 특성 연구

2016 년 2 월

서울대학교 대학원
지구환경과학부 수리지구환경연구실
이 승 현

ABSTRACT

Understanding fluid flow and solute transport in a rough-walled fracture is important in many problems such as petroleum and geothermal reservoir exploitation, geological storage of CO_2 and siting of radioactive waste repositories.

In order to understanding of fracture flow, we conducted the direct measurement of flow velocity across rough-walled fractures at Reynolds number (*Re*) of 0.014 to 0.086. The results were used for an order of magnitude analysis to evaluate assumptions underlying the Stokes and the Reynolds equations, which are derived from simplifying the Navier - Stokes equations. Even at very rough subregions, viscous forces were at least 2 orders of magnitude greater than inertial forces, indicating that the Stokes equations are valid for $Re < 0.1$. However, the assumption made in the derivation of the Reynolds equation that $\partial^2 u_x / \partial z^2$ is dominant over other viscous terms was not satisfied even at moderate roughness for $Re < 0.1$. The Reynolds equation overestimated flow rate.

Also, microscopic observation of solute transport through a rough-walled fracture was made to assess the evolution of eddies and their effect on non-Fickian tailing, A noteworthy phenomenon was observed that as the eddy grew, the particles were initially caught in and swirled around within eddies, and then cast back into main flow channel, which reduced tailing.

This differs from the conventional conceptual model, which presumes a distinct separation between mobile and immobile zones. Fluid flow and solute transport modeling within the 3-D fracture confirmed tail shortening due to mass transfer by advective paths between the eddies and the main flow channel, as opposed to previous 2-D numerical studies that showed increased tailing with growing eddies.

Key words: microPIV, breakthrough curve, rough-walled fracture, eddy flow, Navier-Stokes flow, Reynolds equation, tailing effect

Student Number: 2009 - 20376

TABLE OF CONTENTS

LIST OF FIGURES

CHAPTER I.

CHAPTER II.

CHAPTER III.

LIST OF TABLES

CHAPTER II.

CHAPTER III.

CHAPTER I.

INTRODUCTION

CHAPTER I. INTRODUCTION

1.1 Background theory

Groundwater flow through fractured rocks

At depths of tens to hundreds of meters below the surface, which include fractured consolidated media like fractured bed rock, the matrix has extremely low hydraulic conductivity. This indicates that groundwater migrations through discrete fractures and faults are the dominant mechanism for flow and transport at the crystalline fractured rock medium.

Fractures with large aperture may generate preferential flows, which result in rapid groundwater migration [*Borgne et al.,* 2006; *Myers*, 2012]. Therefore, the hydraulic properties of fractures are important to basic groundwater flow, contaminant transport, cap rock integrity of radioactive waste disposal sites [*Potter et al*., 2004], and carbon dioxide storage sites [*Bigi et al.,* 2013; *Tongwa et al.,* 2013].

Numerous studies of fracture flow have been performed in various scales: micro-scale (e.g. pore scale flow considering the fracture wall boundary), experimental scale to field scale (e. g. fracture connectivity and preferential flow), as shown in Figure 1-1 [*Berkowitz,* 2002]

For a practical point of view, research in field scale, that involves massive heterogeneities have been conducted for characterizing hydraulic properties. However, in order to reveal the fundamental causes of these phenomena, microscopic approaches need to be combined with large scale studies. This means that research related to flows in a single fracture can be a good start for a better understanding of field situations [*Bodin et al.*,2003a, 2003b].

On the field scale, a wide groundwater velocity range through fractured zone is likely to occur due to the various aperture sizes and the hydraulic gradient. Groundwater flow in a porous medium is known to very slow, and it follows darcy's law. In the case of crystalline fractured rock, the rock matrix is impermeable, and the effective fracture porosity is very low (10^{-2} to 10^{-5}).

Thus, despite the fact that the bulk hydraulic conductivity is low, actual flow velocity through a fracture is much greater than the bulk groundwater velocity. Therefore, groundwater flows in fractured rock need to be investigated while considering a wide velocity range.

Figure 1-2 shows a wide fracture flow velocity range which is likely to occur on a field scale based on the cubic law assumption. The average velocity ($\bar{u}_x$) in a single fracture is represented as:

$$\overline{u_x} = -\frac{\rho g e^2}{12\mu}\frac{dh}{dl} \tag{1-1}$$

where, ρ denotes the density, g is the gravitational acceleration, e is the hydraulic aperture, μ is the viscosity, and dh/dl is the hydraulic gradient..

To represent a wide velocity range in a fractured medium, a hydraulic aperture range of 0.1 mm to 1 mm, a natural hydraulic gradient of 0.001 to 0.01, and an artificial hydraulic gradient of 0.05 to 0.2 (e.g., a hydraulic gradient during pumping) were assumed.

In this research, a series of experiment was conducted in velocity range of $1.38 \cdot 10^{-5}$ m/s to $8.3 \cdot 10^{-5}$ m/s (chapter 2, see range a in figure 1-2), and $8.3 \cdot 10^{-5}$ m/s to $1.6 \cdot 10^{-2}$ m/s (chapter 3, see range b in figure 1-2), which include the range of the natural fracture flow velocity and the artificial fracture flow velocity for a fractured rock medium, respectively.

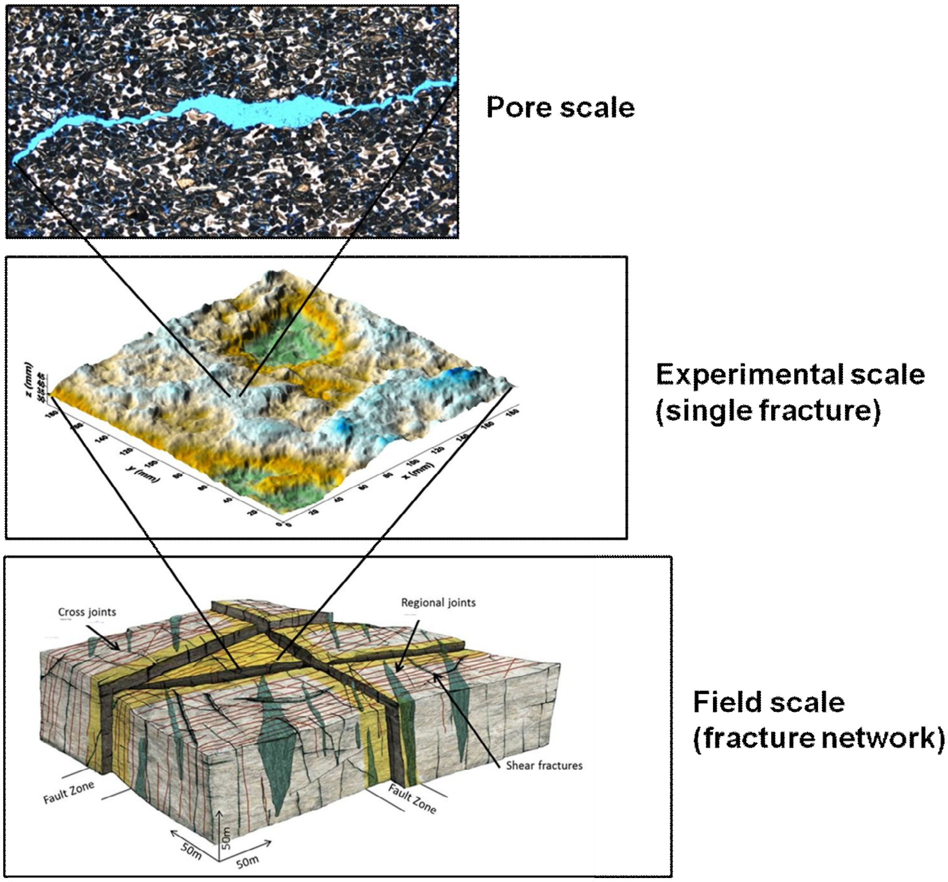

Figure 1-1 Multiscale approaches to understand the flow mechanism in a fractured medium.

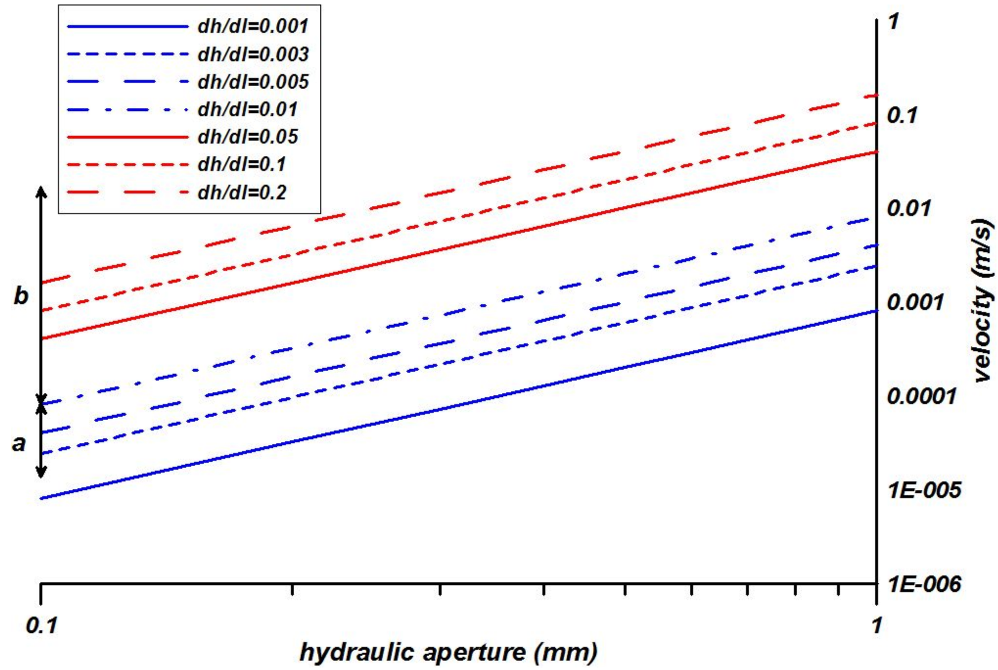

Figure 1-2 Fracture flow velocity range based on the cubic law assumption.

Fluid flow in a single fracture

The cubic law has been widely used to represent groundwater flow in a fractured medium due to its simplicity. It assumes an ideal, parabolic velocity distribution. The flux through the single fracture is proportional to the cube of aperture, and velocity vector magnitudes can exist only in the x - direction (i.e. flow direction) (Figure 1-3).

However, for a real flow system under the subsurface, the fractures are rough around the wall, which makes non-parabolic profiles, form an extremely low velocity zone near the wall. Furthermore, a velocity with regard to the z - direction is generated depending on the roughness, which causes differing fluid flow behaviors when compared to flow from cubic law assumptions. Under the same pressure gradient condition, the flux between parallel-walled cases and rough-walled cases can also be different due to the energy losses by fracture wall roughness.

The exact fluid flow behavior is represented based on the Navier-Stokes equations (N-S equations) [*Zimmerman and Bodvarsson*, 1996]. The N-S equations can be simplified to Stokes and Reynolds equations based on several assumptions for a more efficient application. However, the reduced equations should be applied cautiously since the use of simplified equations for fluid flow and solute transport may lead to different conclusions [*Koyama et al.,* 2008]. The results from the reduced equations might be meaningless if the assumptions do not satisfy the field situations.

The huge differences such in velocity profile deviation, immobile zone generation, and solute mixture come from the wall roughness in a single fracture (Figure 1-3). For this reason, the effect of roughness on the fluid flow and solute transport have been investigated through both numerical approaches [*Boutt et al.*, 2006; *Cardenas et al.*, 2007; *Koyama et al.,* 2008; *Cardenas et al.,* 2009] and experimental approaches [*Hakami and Larsson*, 1996; *Yeo et al.*, 1998; *Nicholl et al.*, 1999].

The numerical simulations based on the N-S equations have a heavy computational problem when the fracture boundary is more complex. Thus, these studies based on the N-S flow in a single fracture are limited to two dimensional (2-D) simulations.

In the previous experimental approaches, due to the difficulty of investigating fracture inside, only the inlet and outlet information were only acquired, which hinders the full understanding of the inner fracture flow mechanism. Therefore, a direct visualization can be more intuitive than previously mentioned approaches for understanding the microscopic phenomena.

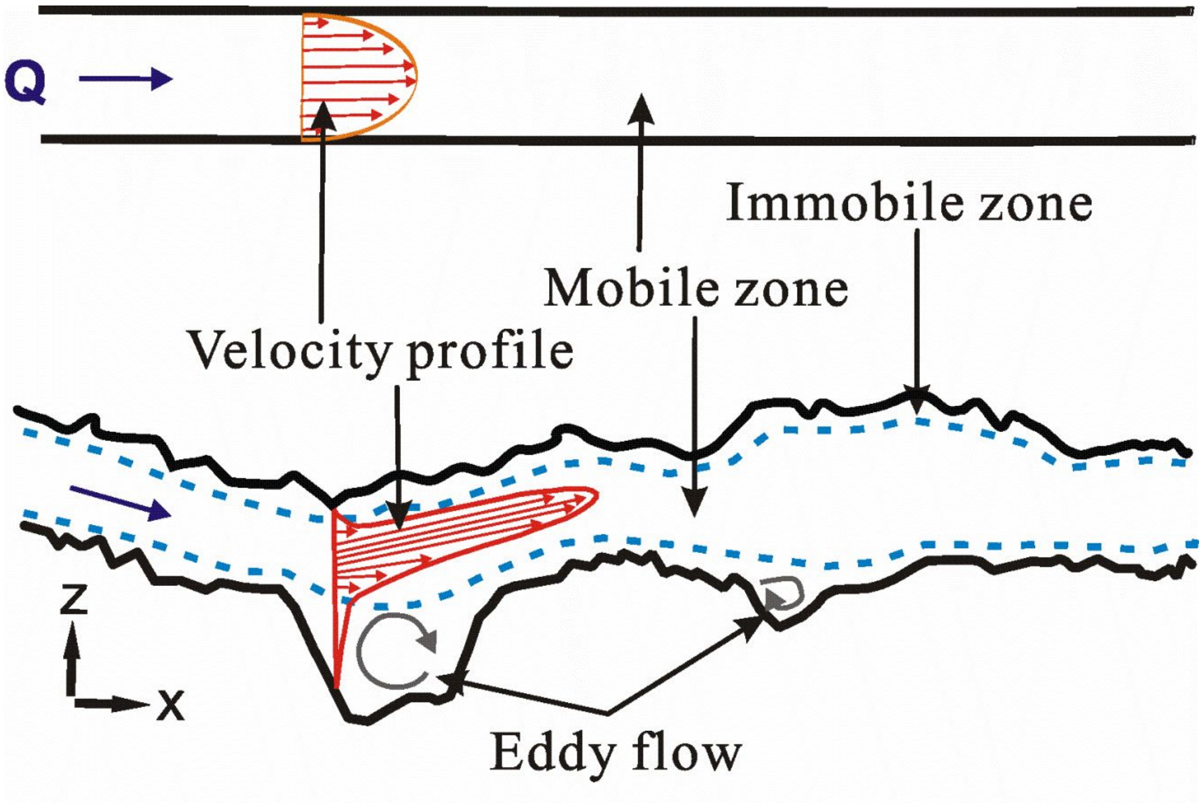

Figure 1-3 Conceptual flow characteristics in a parallel fracture (flow based on cubic law), and in a rough-walled fracture (real flow).

1.2 Objectives of this study

Visualization approaches are useful for interpreting flow and transport phenomena in a single fracture. Directly visualized images that show velocities, solute mixing, and eddy growths can be utilized to analyze the hydraulic characteristics in a single fracture. The objective of this study is to understand the effects of wall roughness on fluid flow and solute transport mechanisms via microscopic observations.

This study is divided into 2 categories: microscopic visualization and numerical simulation (Figure 1-4).

The fluid flow and solute transport through an acrylic single fracture is directly visualized using a microscope with CCD camera and fluorescent materials (fluorescent particles and Rhodamine B). Analysis from the visualized images reveals (1) the velocity distribution changes depending on fracture roughness, (2) the applicability of the reduced equations like Stokes and Reynolds equations, and (3) the solute dispersion characteristics depending on fracture roughness and Reynolds number. The results were compared to numerical simulation results.

In chapter 2, 8 representative subregions in a rough-walled single fracture are selected. The magnitudes of the terms in the N-S equations are calculated from the velocity distributions using microPIV, and quantified at each subregion. The validity of Stokes and Reynolds equations were assessed by analyzing the magnitude of each terms in the Navier-Stokes equations.

In chapter 3, breakthrough curves (BTCs) were plotted from a series of experiments to investigate the solute dispersion in a rough-walled single fracture. Based on the dispersion coefficient changes and the eddy evolution with the increased Reynolds number, the role of eddy flows on solute transport (e.g. tail shortening, Non - Fickian tailing) was investigated. These phenomena are confirmed by the numerical simulations based on N-S equations: 1) a 2-D simulation at identical conditions from the experiment and 2) simulations on an idealized, simple 3-D fracture.

The research will improve our understanding of flow and transport in a highly rough - walled, fractured medium.

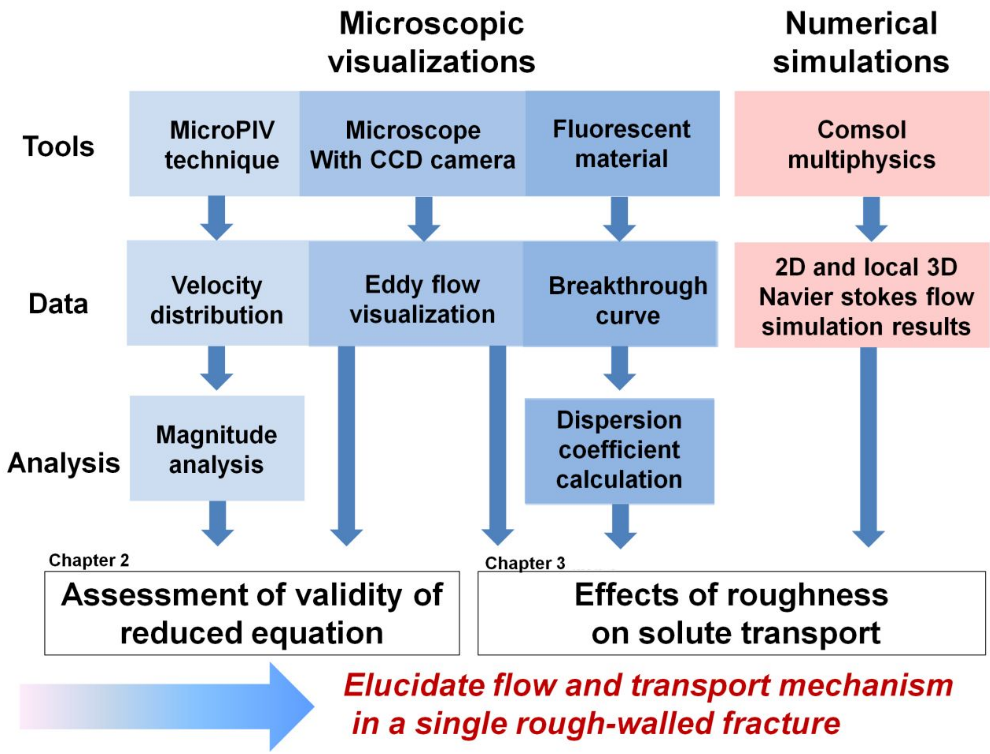

Figure 1-4 Objectives of the study.

CHAPTER 2.

VISUALIZATION OF FLUID FLOW

Validity of Stokes and Reynolds equations for fluid flow through a rough-walled fracture with flow imaging

CHAPTER 2. VISUALIZATION OF FLUID FLOW:

Validity of Stokes and Reynolds equations for fluid flow through a rough-walled fracture with flow imaging

In this chapter, flow characteristics through a single rough-walled fracture are studied. 8 representative subregions in an acrylic rough-walled single fracture are selected considering tortuosity. At each subregion, velocity profiles were acquired, which were used for calculation of the magnitudes of the terms in the N-S equations. Through the magnitude analysis and images of eddy flow growth, validity of the assumptions on Stokes and Reynolds equations were evaluated.

2.1 Introduction

The understanding of fluid flow through a rough-walled fracture is a starting point for a better interpretation of the flow through fracture networks and solute transport. Fluid flow through rough-walled fractures can be fully described by the Navier-Stokes (N-S) equations [*Zimmerman and Bodvarsson*, 1996]. However, the inertia term of the N-S equations, causing fluid flow to be nonlinear, makes the equations very difficult to solve, which naturally leads to the simplification to the Stokes equations and further to the Reynolds equation (or local cubic law) [*Zimmerman and Yeo*, 2000].

The Stokes equations can be obtained by neglecting the inertia term in the N-S equations under the condition of the Reynolds number (Re) << 1 [*Oron and Berkowitz*, 1998; *Zimmerman and Yeo*, 2000; *Brush and Thomson*, 2003], where Re is defined as $\rho u e_m/\mu$, where ρ is density, u is the velocity, e_m is the arithmetic mean aperture, and μ is the viscosity. Although the Stokes equations are a linear form of the N-S equations, their solutions are still difficult to obtain. Further, the geometrical constraint that the aperture varies very gradually reduces the Stokes equations to the more tractable Reynolds equation.

The Reynolds equation has been widely used to quantify fluid flow through rough-walled fractures because of its simplicity [*Brown,* 1987; *Yeo et al*., 1998; *Nicholl et al*., 1999; *Giacomini et al.,* 2008]. However, it has been reported that flow rate predicted by the Reynolds equation was 1.22 - 2.4 times greater than that measured from laboratory flow tests [*Hakami and Larsson*, 1996; *Yeo et al*., 1998; *Nicholl et al*., 1999]. The overestimation of flow rate by the Reynolds equation was ascribed to abrupt aperture change and/or nonlinearity caused by inertial force.

Recent numerical developments have enabled a number of numerical studies using the N-S equations to be conducted for fluid flow through rough-walled fractures [*Brush and Thomson,* 2003; *Zimmerman et al.,* 2004; *Boutt et al*., 2006; *Cardenas et al*., 2007; *Koyama et al.,* 2008; *Cardenas et al*., 2009]. *Zimmerman et al*. [2004] showed that a weak inertial regime existed at Re = 1 to 10, but nonlinear flow became considerable for

Re > 20. However, it was reported that the recirculation zones were generated at large aperture area even for Re < 1 [*Boutt et al*., 2006; *Cardenas et al*., 2007], meaning that nonlinear flow could exist at Re < 1. The studies also demonstrated that the Reynolds equation, which itself tends to overestimate the flow, needed to be modified with a geometric mean aperture, arithmetic mean aperture, true aperture (measured normal to segment orientation), surface roughness factor, tortuosity, or friction factor [*Ge*, 1997; *Oron and Berkowitz*, 1999; *Brush and Thomson,* 2003; *Konzuk and Kueper, 2004; Mallikamas and Rajaram*, 2010; *Qian et al*., 2011].

Geometric and kinematic constraints have been suggested for the validity of the Reynolds equation: $\Lambda > 3e_m$ [*Zimmerman and Yeo*, 2000], Re < 1 [*Renshaw et al.*, 2000; *Brush and Thomson,* 2003; *Konzuk and Kueper, 2004*], $Re\ b_m / \Lambda < 1$ [*Brush and Thomson,* 2003], and $Re\ \sigma / b_m < 1$ [*Brush and Thomson,* 2003], where, Λ is wave length of dominant aperture variation and σ is the standard deviation of apertures, and *Renshaw et al.*[2000] used the hydraulic aperture for Re. There is a general consensus that the Reynolds equation is valid for rough-walled fractures at Re < 1. However, *Nicholl et al*. [1999] found that the Reynolds equation still over-predicted flow rate by 22 - 47%, especially at Re = 0.063 to 4.3. It was not clear whether this overestimation at Re < 1 was due to nonlinearity and/or abrupt aperture changes. Moreover, the validity of the Reynolds equation even for low Re (< 1), at which fluid flow in rough-walled fractures mainly takes place, still remains questioned and unresolved.

In this study, the first direct microscopic observation of flow phenomena across a rough-walled fracture such as velocity vector and eddy structures was made, which has been carried out only numerically in the previous studies to investigate the geometrical effect on fluid flow [*Boutt et al.,* 2006, *Cardenas et al.,* 2007; *Chaudhary et al.,* 2011, 2013; *Qian et al.,* 2012]. Flow velocity measured directly from a rough-walled fracture using microscopic particle image velocimetry (PIV) enables the first evaluation of relative magnitude between inertial and viscous force terms of the N-S equations and between the viscous force terms of the Stokes equations, which contributes to the examination of the validity of the Stokes and the Reynolds equations for fluid flow through rough-walled fractures at low *Re.*

2.2 Governing Equations of Fluid Flow

2.2.1 From the N - S to the Stokes Equations

At steady state, fluid flow through the fracture is governed by the following the N-S equations:

$$\rho(\mathbf{u}\cdot\nabla)\mathbf{u} = \mu\nabla^2\mathbf{u} - \rho g\nabla h\ , \tag{2-1}$$

where ρ is the density, g is the gravitational acceleration, $\mathbf{u}$ is the velocity vector, μ is the viscosity, and h is the hydraulic head. The inertia term on the left-hand side makes the N-S equations nonlinear. The first term on the right represents viscous forces. For the two-dimensional flow, equation (2-1) can be reduced to

$$\rho\left(u_x\frac{\partial u_x}{\partial x} + u_z\frac{\partial u_x}{\partial z}\right) = \mu\left(\frac{\partial^2 u_x}{\partial x^2} + \frac{\partial^2 u_x}{\partial z^2}\right) - \rho g\frac{\partial h}{\partial x} \tag{2-2}$$

$$\rho\left(u_x\frac{\partial u_z}{\partial x} + u_z\frac{\partial u_z}{\partial z}\right) = \mu\left(\frac{\partial^2 u_z}{\partial x^2} + \frac{\partial^2 u_z}{\partial z^2}\right) - \rho g\frac{\partial h}{\partial z}\ . \tag{2-3}$$

To neglect inertial terms, viscous forces should be strong enough to damp down any perturbations from the linear laminar flow field [*Zimmerman and Yeo,* 2000]:

$$\boldsymbol{mag}\left(\mu\frac{\partial^2 u_x}{\partial x^2},\ \mu\frac{\partial^2 u_x}{\partial z^2}\right) >> \boldsymbol{mag}\left(\rho u_x\frac{\partial u_x}{\partial x},\ \ \rho u_z\frac{\partial u_x}{\partial z}\right), \tag{2-4}$$

$$\boldsymbol{mag}\left(\mu\frac{\partial^2 u_z}{\partial x^2},\ \mu\frac{\partial^2 u_z}{\partial z^2}\right) >> \boldsymbol{mag}\left(\rho u_x\frac{\partial u_z}{\partial x},\ \ \rho u_z\frac{\partial u_z}{\partial z}\right) \tag{2-5}$$

where ***mag*** indicates the magnitude of each term inside the bracket. Then, the N-S equations can be linearized to the Stokes equations:

$$\mu\left(\frac{\partial^2 u_x}{\partial x^2}+\frac{\partial^2 u_x}{\partial z^2}\right)=\rho g\frac{\partial h}{\partial x}, \tag{2-6}$$

$$\mu\left(\frac{\partial^2 u_z}{\partial x^2}+\frac{\partial^2 u_z}{\partial z^2}\right)=\rho g\frac{\partial h}{\partial z} \tag{2-7}$$

2.2.2 From the Stokes to the Reynolds Equations

Simplification of the Stokes equations to the Reynolds equations requires further constraints that the second-order partial derivative of u_x with respect to z dominates other viscous forces of equations (2-6) and (2-7):

$$\boldsymbol{mag}\left(\frac{\partial^2 u_x}{\partial z^2}\right) >> \boldsymbol{mag}\left(\frac{\partial^2 u_x}{\partial x^2}\right), \text{ and } \boldsymbol{mag}\left(\frac{\partial^2 u_x}{\partial z^2}\right) >> \boldsymbol{mag}\left(\frac{\partial^2 u_z}{\partial x^2} + \frac{\partial^2 u_z}{\partial z^2}\right) \tag{2-8}$$

The constraints (equation (2-8)) can be achieved when the aperture varies gradually. If the above conditions are satisfied, the Stokes equations can be simplified to

$$\mu\left(\frac{\partial^2 u_x}{\partial z^2}\right) = \rho g \frac{\partial h}{\partial x}. \tag{2-9}$$

Integration of equation (2-9) over z with no slip boundary condition and the continuity equation results in the one-dimensional Reynolds equation [*Zimmerman and Bodvarsson*, 1996]:

$$\frac{\partial}{\partial x}\left(\frac{\rho g e^3(x)}{12\mu}\frac{\partial h}{\partial x}\right) = 0, \tag{2-10}$$

where e is the aperture. Equation (2-10) can be viewed as a local version of the cubic law.

Abrupt variation of the apertures causes $\frac{\partial^2 u_x}{\partial x^2}$ to increase enough to be comparable to $\frac{\partial^2 u_x}{\partial z^2}$, leading to failure of the condition (equation (2-8)) required for the validity of the Reynolds equations, Thus, if the aperture changes abruptly, the Reynolds equation tends to overestimate flow rate.

2.2.3 Use of the governing equations for fracture flow

As noted in Chapter 2.2.1 and Chapter 2.2.2, complex equations are simplified based on several assumptions. Figure 2-1 shows the representation of the fracture wall boundary (left) for each equation and its application to simulate a groundwater flow (right).

The N-S equation and the Stokes equation require continuous information about the fracture wall geometry to represent the exact behavior of water flows (figure 2-1a). In this case, numerical simulations through complex and irregular 3D geometry domains are difficult and require heavy computations. For this reason, simulations through the 2D domain structure are mainly performed to investigate fluid flows in the case of a single fracture [*Zou et al.,* 2015].

For the Reynolds equation, the aperture distribution in a fracture can be discretely defined, as shown in Figure 2-1b. The Reynolds equation assumes a single aperture value at each element, and it satisfies the cubic law assumption, locally. Generally, the Reynolds equation or the modified Reynolds equation is widely used to simulate fracture flows in the 3D domain of a single fracture while taking into account the aperture heterogeneity [*Ishibashi et al,* 2012].

For a field-scale simulation including a discrete fracture network (DFN), characterizing the aperture distribution and implementing it into the model are impossible. In this case, a single representative hydraulic aperture value per single fracture is defined as shown in figure 2-1c [*Blessant et al.,* 2011]. The simplified form of the equation is more applicable to simulate a fracture flow on a large scale.

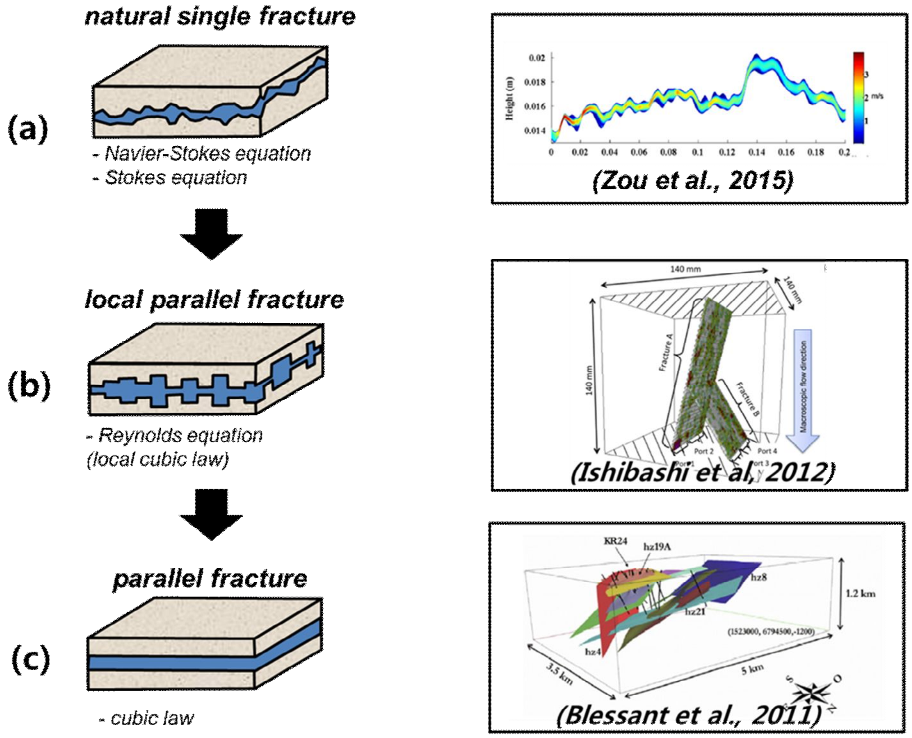

Figure 2-1 Conceptualization from a natural to a parallel plate [Modified from *Dietrich et al.,* 2005].

2.3 Experimental Methods

Micro Particle Image Velocimetry (MicroPIV) technique

MicroPIV technique is an optical method for the fluid visualization to obtain velocity vectors using the continuous snapshots with time interval (Δt) (Figure 2-2). The frames of captured images are split into a number of interrogation areas (Figure 2-3). As a tracer, fluorescent particles (various diameters from nanometer to micrometer scale for the tracking purposes) are mixed with deionized water. Under the specified flow condition, the mixed particles move along with water flow. By calculating the distance of particles' movement between the snapshots, representative velocity in the interrogation area can be determined.

Through the cross-correlation of the images between two snapshots at interrogation areas, displacement of particles is adopted as the movement distance during the Δt between adjacent snapshots (Figure 2-2). Finally, velocity sets from the hundreds of snapshots are averaged to reduce the unexpected movement by Brownian motion (i.e. particle movement by diffusion mechanism).

The micro-PIV system in this study consists of an inverted microscope (Olympus IX-50), syringe pump, CCD camera, mercury lamp, and computer (Figure 2-3b), which has been used before in the field of fluid mechanics [*Li and Olsen*, 2006; *Zheng and Silber-Li*, 2008]. Deionized water mixed with 1 μm sized fluorescent particles was injected into the rough-walled acrylic fracture using a syringe pump at different injection rates. The arithmetic mean aperture and injection flow rate were used to calculate the representative *Re* for the whole fracture. Continuous snap shots were captured using a CCD camera, and velocity vectors in the observed frame were calculated by analyzing the relative movement of particles between snap shots with time intervals. Velocity vectors were measured at every 0.05 mm in both x and z directions. However, at high velocity, particles passing through the observed frame were too fast to trace (i.e., observed as a line rather than a dot), preventing calculating representative velocity vectors. The optimum *Re* at which flow velocity could be measured with our micro-PIV system is limited to 0.086.

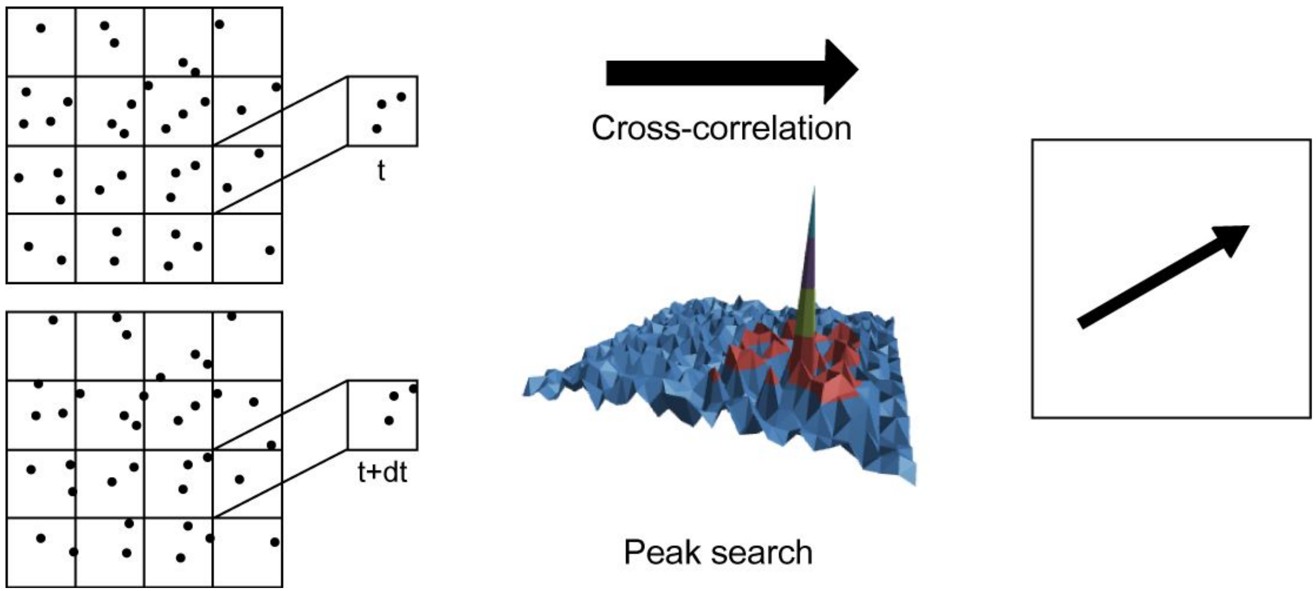

Figure 2-2 Principle of Micro PIV technique to obtain the velocity vectors at an each interrogation area.

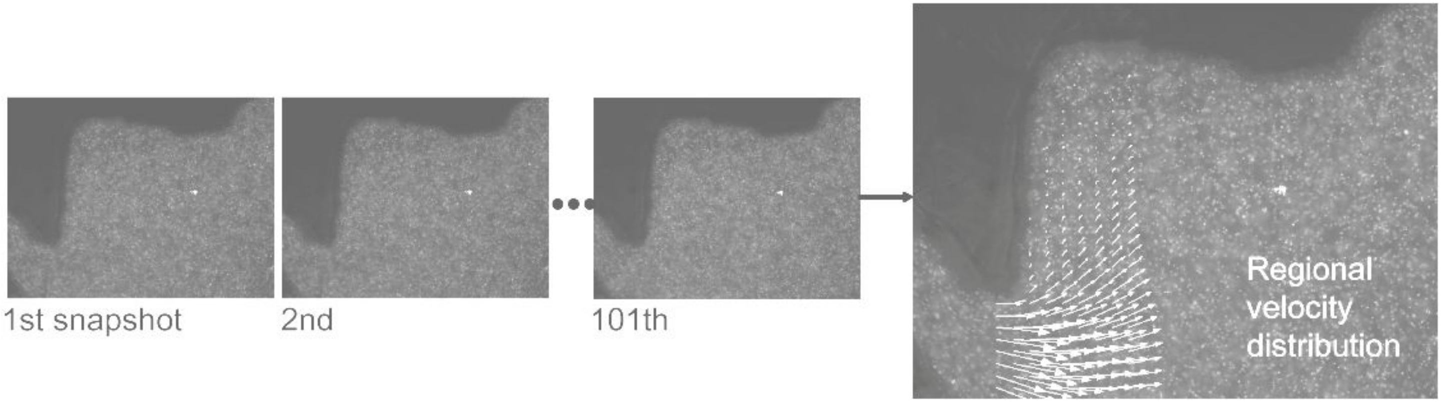

Figure 2-3 Examples of the velocity field acquisition near the top boundary of subregion e at the rough-walled fracture sample.

Properties of the rough-walled fracture sample

Both surfaces of a rough-walled fracture were scanned and were then duplicated on acrylics using a numerically controlled computer modeling machine, which produced a rough-walled acrylic fracture that was 20 cm long. The aperture varied from 387 to 2487 μm with an arithmetic mean aperture and a standard deviation of 1030 μm and 411 μm, respectively (Figure 2-4a and Figure 2-4c).

Velocity vectors, measured at eight representative subregions of the rough-walled fracture: *a* to *h* (Figure 2-4a). The subregions were classified into smooth-walled regions (c and h: tortuosity < 1.2), moderately rough-walled regions (a, b, d, and g: 1.2 < tortuosity< 2.0), and highly rough-walled fracture regions (e and f: 2.0 < tortuosity), where tortuosity is defined in Figure 2-4. Table 2-1 represents the local arithmetic mean aperture, standard deviation, and tortuosity of top and bottom boundary. A parallel-walled fracture with an aperture of 1100 μm was also prepared, and flow velocities were measured for comparison purposes. The measurements were carried out at *Re* from 0.014 to 0.086 for both rough- and parallel-walled fractures. Flow phenomenon such as eddy structures were visualized experimentally up to *Re* = 17.1.

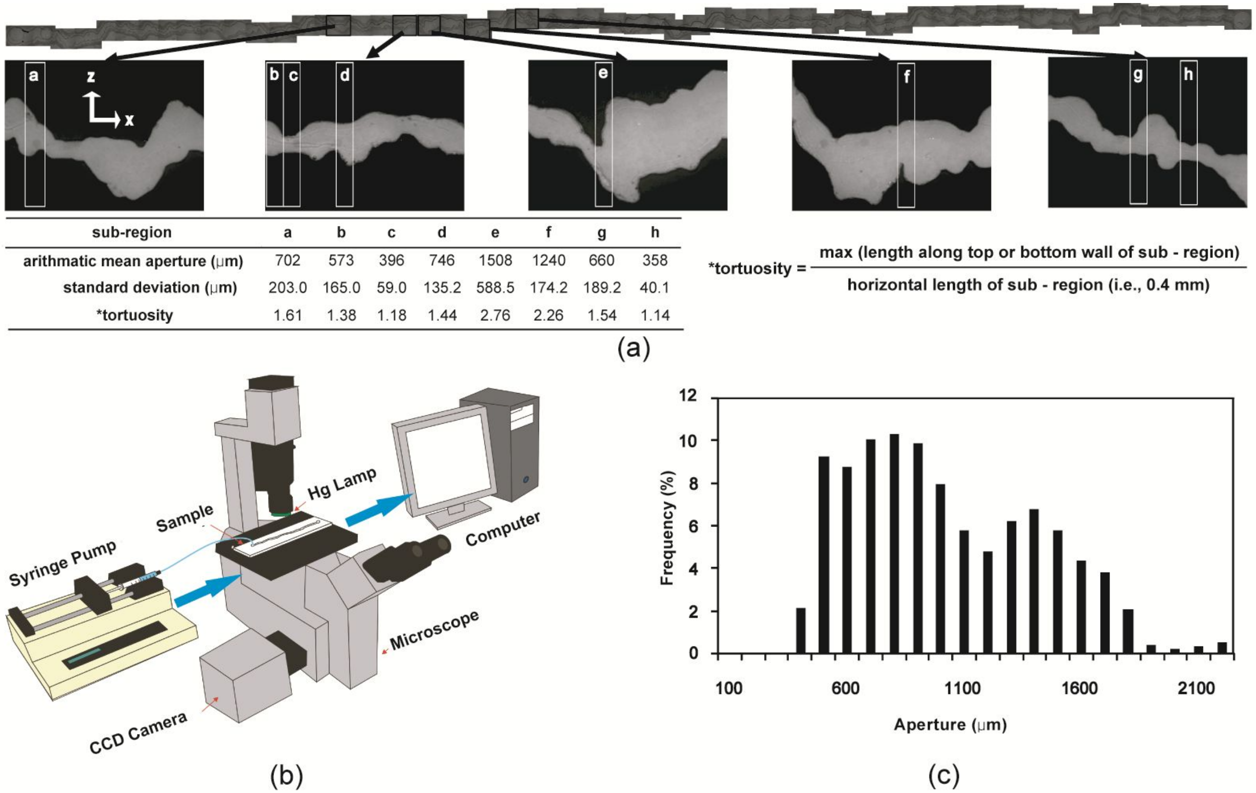

sub-region	a	b	c	d	e	f	g	h
arithmatic mean aperture (μm)	702	573	396	746	1508	1240	660	358
standard deviation (μm)	203.0	165.0	59.0	135.2	588.5	174.2	189.2	40.1
*tortuosity	1.61	1.38	1.18	1.44	2.76	2.26	1.54	1.14

Figure 2-4 (a) Eight representative subregions of the rough-walled fracture, (b) the experimental setup of micro-PIV, and (c) histogram of aperture.

Table 2-1 Basic statistics at eight representative subregions

Sub-region	Local mean aperture (micrometer)	Local Standard Deviation (micrometer)	Tortuosity (top) (dimensionless)	Tortuosity (bottom) (dimensionless)
a	701.5	202.98	1.61	1.36
b	573.3	164.98	1.38	1.10
c	396.3	58.96	1.18	1.03
d	746.2	135.15	1.10	1.44
e	1507.6	588.51	2.76	1.67
f	1239.8	174.21	1.10	2.26
g	660.2	189.16	1.54	1.08
h	357.8	40.13	1.14	1.09

2.4 Results

2.4.1 Validity of the Stokes equations

To assess the validity of stokes equations, the velocity vectors for all the subregions (a to h) at *Re* = 0.014, 0.029 and 0.086 are measured (Figure 2-5). Velocity vectors, measured at *Re* = 0.029 for a subregion of the parallel-walled fracture and subregion f (see Figure 2-4a for locations of subregions) of the rough-walled fracture with micro-PIV, are represented in Figures 2-7a and 2-7b, respectively. In contrast to the parabolic velocity profile in a parallel-walled fracture, a large low- velocity zone was observed near the bottom wall of the rough-walled fracture, indicating a nonparabolic velocity distribution.

According to *Lee et al.* [2007], slip occurs under the condition of a hydrophobic surface. Our constructed acrylic micromodel, having the characteristics of a hydrophobic surface, is quite different from the surface of natural rock, which is assumed to be hydrophilic. Therefore, the slip induces a non-zero velocity near the fracture wall, which has the potential to influence measurement of velocity distributions. Figure 2-6a shows directly visualized velocity distributions using the microPIV technique under the condition of a parallel fracture wall.

In our measuring system, the length of each interrogation area is 50 micrometers, implying that the average velocity in a rectangular area (i.e., one velocity vector per interrogation area 50μm × 50μm in size) is represented. Therefore, an investigation of the exact behavior at the point of a fracture wall is impossible at our resolution. Considering the principle of the microPIV method, the measured velocity near the fracture wall is likely to be faster than the actual velocity.

However, the measured velocity profile appears to be parabolic, and np noticeable slip was observed, as shown in figure 2-6b. Although slip occurred on our acrylic surface, the effect was sufficiently negligible, meaning that the slip did not cause an error in the magnitude analysis conducted in this experiment.

The measured velocity vectors were used to evaluate the magnitude of the inertial force and viscous force terms shown in equation (2-4) and (2-5). The magnitudes of the terms were approximated by constructing a finite difference equation replacement for the second-order partial differential equations.

The magnitudes of the inertial force terms and viscous force terms at each interrogation area of row i, column j were defined using adjacent velocity vectors (Equation (2-11) to Equation (2-14)).

$$\boldsymbol{mag}_{i.j}\left(\rho u_x \frac{\partial u_x}{\partial x}\right) = \rho u_x \frac{u_{x(i+1,j)} - u_{x(i-1,j)}}{2\Delta x} \qquad (2\text{-}11)$$

$$\boldsymbol{mag}_{i.j}\left(\rho u_z \frac{\partial u_x}{\partial z}\right) = \rho u_z \frac{u_{x(i,j+1)} - u_{x(i,j-1)}}{2\Delta z} \qquad (2\text{-}12)$$

$$\boldsymbol{mag}_{i.j}\left(\mu\frac{\partial^2 u_x}{\partial x^2}\right)=\mu\frac{u_{x(i-1,j)}-2u_{x(i,j)}-u_{x(i+1,j)}}{(\Delta x)^2} \tag{2-13}$$

$$\boldsymbol{mag}_{i.j}\left(\mu\frac{\partial^2 u_x}{\partial z^2}\right)=\mu\frac{u_{x(i,j-1)}-2u_{x(i,j)}-u_{x(i,j+1)}}{(\Delta z)^2} \tag{2-14}$$

The magnitudes of inertial and viscous forces estimated at each measuring grid point were added up for the whole subregion, which was taken as the representative magnitude of the subregion (Table 2-2).

For the parallel-walled fracture, the magnitude of the inertial forces fell far below that of the viscous forces by as low as 10^{-4} at *Re* = 0.014 to 10^{-3} at *Re* = 0. 086 (Figure 2-7a). Even for the highly rough-walled subregion, f, the magnitudes of the inertial forces were at least 10^{-3} to 10^{-2} times smaller for the range of *Re* = 0.014 to 0.086 than that of viscous forces (Figure 2-7b).

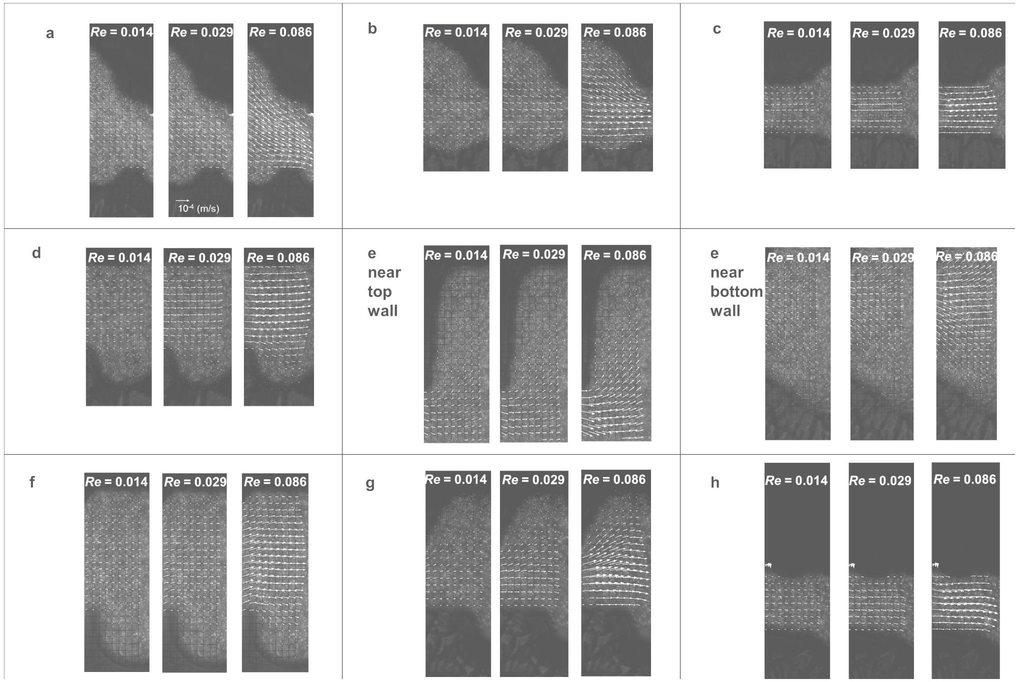

Figure 2-5 Velocity vectors measured by microPIV technique for all subregions a to h at *Re* 0.014, 0.029 and 0.086. The letters of a to h in the figures represent the relevant sub-regions (i.e. a for subregion a), and the velocity vectors around the upper and bottom walls of subregion e are shown in separate images. The horizontal scale of each sub-region is 0.5 mm and the y axis is on the same scale

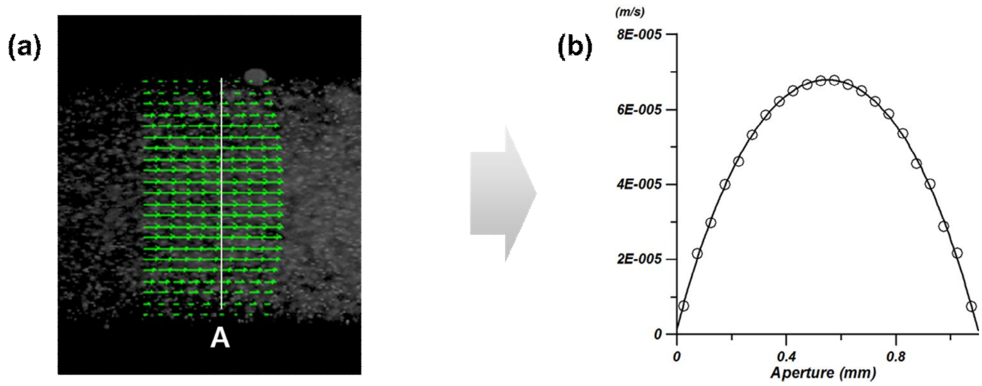

Figure 2-6 (a) Visualized velocity distributions using the microPIV technique under the condition of parallel fracture wall, and (b) velocity distributions at vertical section A.

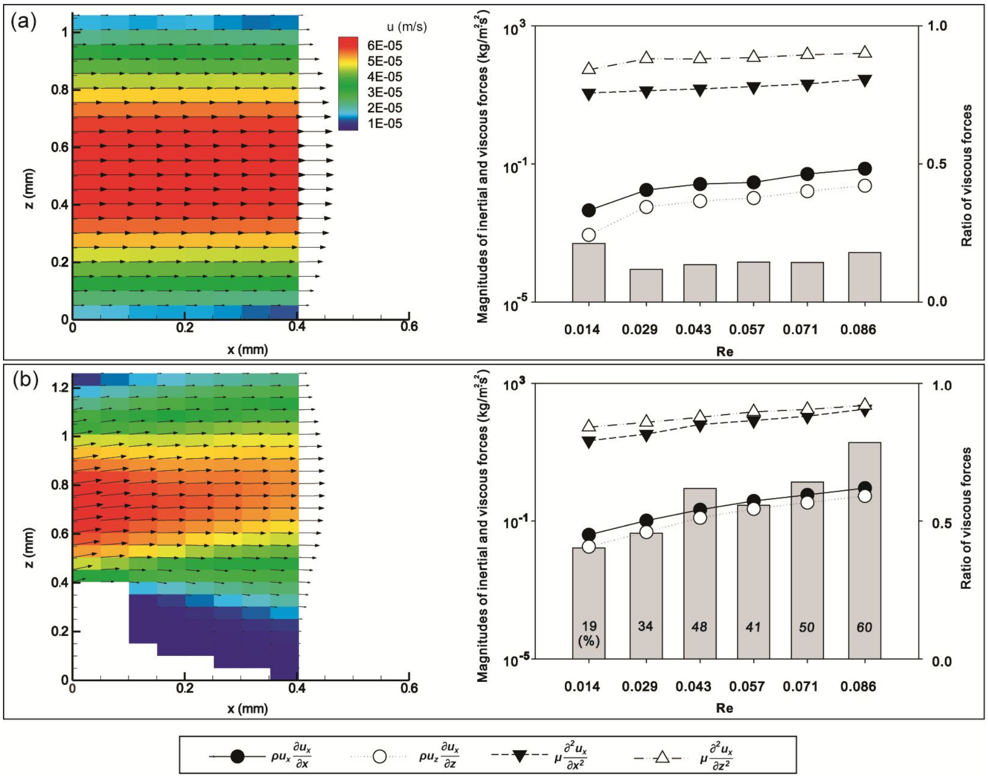

Figure 2-7 (a) Measured velocity vectors and the magnitude of inertial and viscous force terms in the parallel-walled fracture at *Re* = 0.029 and (b) those in subregion f of the rough-walled fracture at *Re* = 0.029. The bar represents the ratio of viscous forces, and the number in the bar indicates the estimated overestimation of flow rate by the Reynolds equation.

Table 2-2 Magnitude of inertial force and viscous force terms in equations ((2-2) and (2-3)). The complete data of the magnitudes and overestimations at sub regions presented in Figure 2-8.

Sub-regions	**Reynolds number**	**Terms in equation (2-2) (kg/m²·s²)**				**Terms in equation (2-3) (kg/m²·s²)**			
		$\rho u_x \frac{\partial u_x}{\partial x}$	$\rho u_z \frac{\partial u_x}{\partial z}$	$\mu \frac{\partial^2 u_x}{\partial x^2}$	$\mu \frac{\partial^2 u_x}{\partial z^2}$	$\rho u_x \frac{\partial u_z}{\partial x}$	$\rho u_z \frac{\partial u_z}{\partial x}$	$\mu \frac{\partial^2 u_z}{\partial x^2}$	$\mu \frac{\partial^2 u_z}{\partial z^2}$
a	**0.014**	0.129	0.096	32.180	67.468	0.078	0.066	27.695	46.048
	0.029	0.334	0.246	49.270	102.881	0.203	0.169	48.368	71.170
	0.086	2.327	1.836	206.806	363.955	1.313	1.304	183.605	243.451
b	**0.014**	0.090	0.063	23.515	71.607	0.050	0.026	22.766	35.825
	0.029	0.257	0.187	40.500	127.735	0.117	0.068	35.736	60.951
	0.086	1.691	1.302	166.957	368.143	0.910	0.501	122.846	160.710
c	**0.014**	0.031	0.009	17.229	99.880	0.039	0.001	9.296	7.992
	0.029	0.091	0.028	29.507	146.280	0.131	0.003	18.493	15.476

	0.086	0.586	0.220	111.406	460.420	0.900	0.029	63.671	71.053
d	**0.014**	0.021	0.013	18.408	62.237	0.037	0.001	11.755	10.621
	0.029	0.072	0.055	37.136	108.536	0.165	0.008	31.258	24.394
	0.086	0.628	0.448	143.196	294.961	1.289	0.061	105.965	68.914
e	**0.014**	0.056	0.039	32.122	56.192	0.071	0.029	31.660	34.505
	0.029	0.160	0.111	49.880	93.723	0.211	0.049	48.213	64.980
	0.086	1.056	0.765	168.381	260.480	1.455	0.329	140.405	170.584
f	**0.014**	0.040	0.018	20.973	52.168	0.058	0.003	19.627	14.105
	0.029	0.102	0.048	32.586	71.568	0.166	0.010	36.678	24.917
	0.043	0.211	0.123	61.762	100.044	0.373	0.030	58.154	43.501
	0.057	0.378	0.223	80.418	144.355	0.619	0.055	72.210	66.276
	0.071	0.569	0.340	107.882	168.389	0.938	0.079	92.747	85.437
	0.086	0.893	0.527	172.650	220.356	1.397	0.123	117.328	103.098
g	**0.014**	0.045	0.026	21.288	57.049	0.045	0.008	19.567	20.354

	0.029	0.176	0.112	49.531	107.936	0.195	0.032	48.135	39.758
	0.086	1.377	1.015	198.362	361.465	1.750	0.301	149.171	122.955
h	**0.014**	0.037	0.018	12.702	57.544	0.037	0.004	13.308	12.709
	0.029	0.160	0.089	30.801	115.685	0.155	0.023	26.652	37.826
	0.086	1.264	0.708	140.321	415.512	1.135	0.171	93.130	146.978

The magnitude ratio of inertial forces to viscous forces ranged from 0.0003 (at subregion c) to 0.0023 (at subregion a) at Re = 0.014, 0.0007 (at subregion c) to 0.0038 (at subregion a) at Re = 0.029, and 0.0014 (at subregion c) to 0.0073 (at subregion a) at Re = 0.086 (Figure 2-8). For the rough-walled fracture, the magnitude of the inertial forces did not exceed to 0.7% of that of the viscous forces. These results indicated that inertial forces were small enough to be neglected. Thus, the simplification from the N-S equation to the Stokes equation can be justified for low Re (< 0.1). The complete magnitude data of the inertial and the viscous forces are provided in Table 2-2.

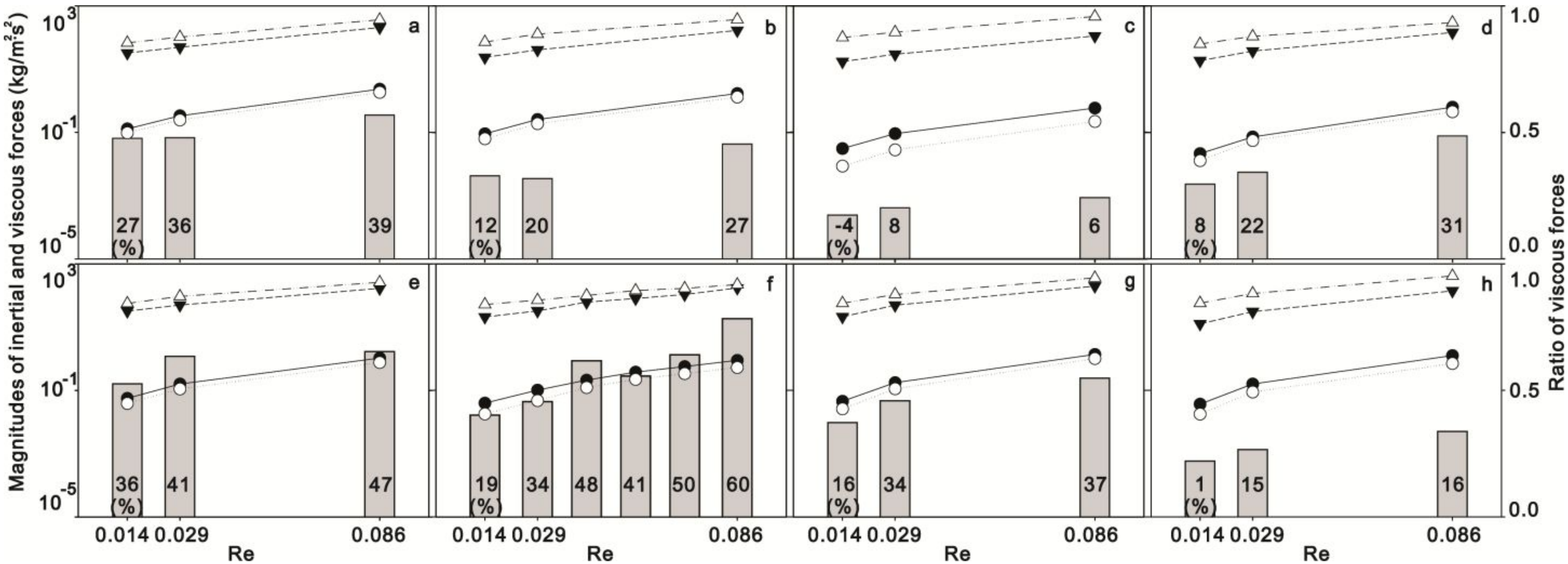

Figure 2-8 Magnitude of inertial force and viscous force terms estimated at the various sub-regions of the rough-walled fracture. Refer to the legend shown in Figure 2-7. The letter in the upper right corner of each box represents the sub-region of the rough-walled fracture.

Although the velocity measurement was limited to low *Re* in our microPIV system, flow phenomena were observed for *Re* > 0.1 through rough-walled fractures. The start of a recirculation zone (eddy) was observed near the rough wall at *Re* = 8.6 (not for *Re* = 5), and it became enlarged with an increase in flow velocity (Figure 2-9), indicating that linear flow could prevail for *Re* < 1. Together with the magnitude comparison between the inertial and viscous force terms, the microscopic observation showed that nonlinear flow did not occur, and the Stokes equations can be used as replacement for the N-S equations for *Re* < 1.

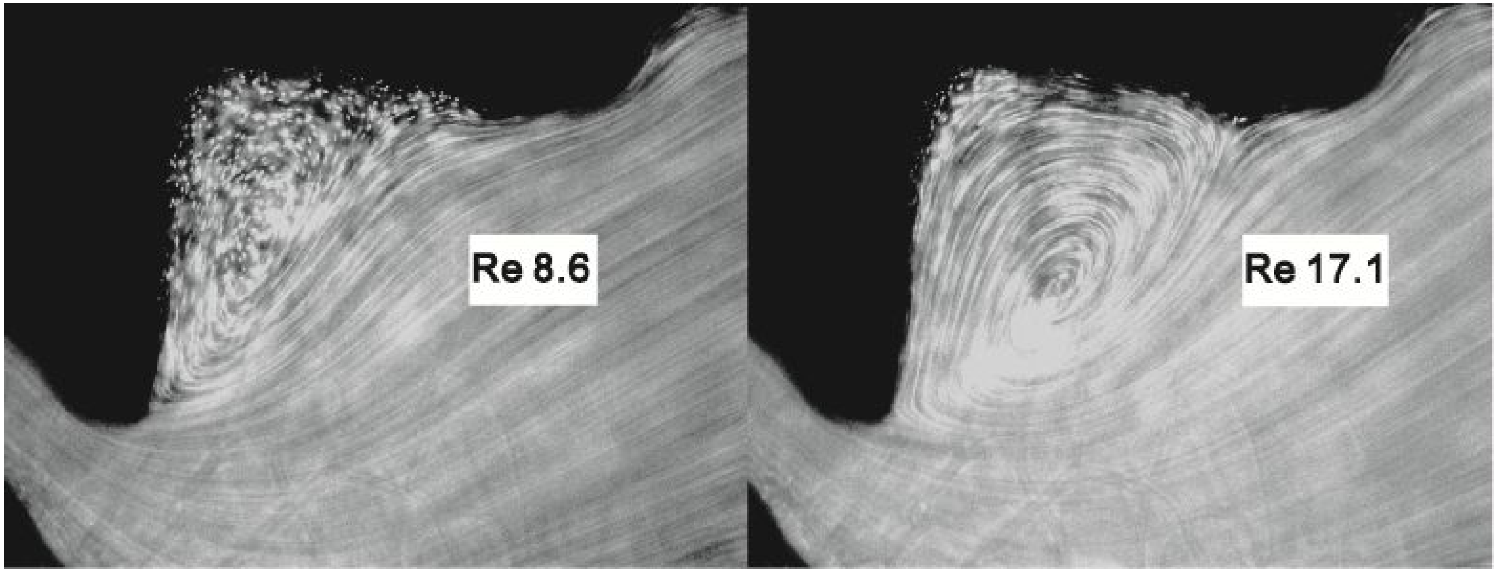

Figure 2-9 Microscopic observation of the generation of recirculation zone at *Re* = 8.6, and its enlargement with an increase of *Re* to 17.1 at the sub-region e.

2.4.2 Validity of the Reynolds Equation

It is known that the Reynolds equation tends to overpredict the flow rate when aperture changes abruptly and/or nonlinear flow occurs. As analyzed above, abrupt aperture change can be a cause of the overestimation of fluid flow by the Reynolds equation for *Re* < 1 rather than nonlinearity. This can be analyzed by evaluating equation (2-8) at the sub-regions representing various roughness conditions.

Figure 2-7a shows the viscous forces estimated for the parallel-walled fracture, showing that the ratio of magnitude of $\partial^2 u_x / \partial x^2$ to that of $\partial^2 u_x / \partial z^2$ ranged from 0.12 to 0.21 for *Re* = 0.014 to 0.086. The viscous force with regard to *x*, $\partial^2 u_x / \partial x^2$, should be theoretically zero for a parallel-walled fracture. This non-zero value is very likely due to measurement error. This ratio was taken into account for later analysis for the rough-walled fracture.

For the rough subregion, f, the ratio of $\partial^2 u_x / \partial x^2$ to $\partial^2 u_x / \partial z^2$ increased from 0.40 to 0.78 with an increase in *Re* of 0.014 to 0.086 (Figure 2-7b). The measured ratio was higher than 0.1, suggested by *Zimmerman and Yeo* [2000], even though the above measurement error was taken into account. Figure 2-8 shows the ratio of viscous forces at various roughness and velocity conditions. For all the observed sub-regions, the magnitude ratio of $\partial^2 u_x / \partial x^2$ to $\partial^2 u_x / \partial z^2$ was 0.17 (subregion c) to 0.57 (subregion e) at *Re* = 0.014, 0.20 (subregion c) to 0.53 (subregion e) at *Re* = 0.029, and

0.24 (subregion c) to 0.78 (subregion f) at *Re* = 0.086. It is clear that the ratio increases with increasing roughness.

The magnitude of $\partial^2 u_z / \partial x^2 + \partial^2 u_z / \partial z^2$ becomes larger than that of $\partial^2 u_x / \partial z^2$ (see Table 2-2) at the rough-walled subregions a and e, while $\partial^2 u_x / \partial z^2$ prevails over the other viscous forces at the smooth-walled subregion c. This magnitude analysis indicates that the constraints (equation (2-8)) for the simplification of the Stokes to the Reynolds equations are not satisfied for $Re < 0.1$, when the roughness varies significantly along with the x-direction.

2.4.3 Quantifying the Overestimation by the Reynolds Equations

An attempt was made to quantify the overestimation by the Reynolds equation. The average value of u_z are relatively small compared to that of u_x except to subregion e, where strong upward flows are developed (Table 2-3). As its positive value for the fracture dipping upward offset its negative ones when the fracture dips downward, the average value of u_z is likely vanish over the entire fracture plane. The average value of u_z measured over eight subregions is 1 order smaller than that of u_x, and it seems reasonable to calculate the volumetric flux using u_x. For the Reynolds equation, average velocity ($\bar{u}_x$) across the aperture can be calculated by [*Zimmerman and Bodvarsson*, 1996].

$$\overline{u_x} = -\frac{\rho g e^2}{12\mu}\frac{dh}{dx} \tag{2-15}$$

Because of very low *Re* condition (< 0.1) in the experiment, the hydraulic head gradient could not be measured. Instead, the head gradient was estimated using measured velocity vectors. The head gradient in the Stokes equation (equation 2-6) and the Reynolds equation (equation 2-9) was substituted into equation (2-15), yielding the volumetric flux through the fracture with a width *w* (perpendicular to the x-z plane):

$$Q = \overline{u_x} e_{\mathrm{Rey}} w = -\frac{e_{\mathrm{Rey}}^3 w}{12}\left(\frac{\partial^2 u_x}{\partial z^2}\right) \tag{2-16}$$

$$Q = \overline{u_x} e_h w = -\frac{e_h^3 w}{12}\left(\frac{\partial^2 u_x}{\partial x^2} + \frac{\partial^2 u_x}{\partial z^2}\right). \tag{2-17}$$

where e_{Rey} and e_h are hydraulic apertures estimated by the Reynolds equation and the Stokes equation. Equation (2-17) has an additional viscous term of $\partial^2 u_x / \partial x^2$, which cannot be neglected when the roughness varies. Thus, as the roughness increases, equation (2-17) yields a smaller hydraulic aperture than equation (2-16). Equating the two equations and correcting the measurement error at the parallel-walled fracture, the overestimation rate can be estimated:

$$\frac{e_{\mathrm{Rey}}^3}{e_h^3} = \left(\frac{\mathbf{mag}\left(\mu \frac{\partial^2 u_x}{\partial x^2}\right) + \mathbf{mag}\left(\mu \frac{\partial^2 u_x}{\partial z^2}\right)}{\mathbf{mag}\left(\mu \frac{\partial^2 u_x}{\partial z^2}\right)}\right) - \left(\frac{\mathbf{mag}\left(\mu \frac{\partial^2 u_x}{\partial x^2}\right)_{Parallel} + \mathbf{mag}\left(\mu \frac{\partial^2 u_x}{\partial z^2}\right)_{Parallel}}{\mathbf{mag}\left(\mu \frac{\partial^2 u_x}{\partial z^2}\right)_{Parallel}}\right)$$

(2-18)

Table 2-3 Average measured velocities ($\bar{u}_x$, $\bar{u}_z$) at each subregions, ($\bar{u}_x$: average velocity in the x- direction $\bar{u}_z$: average local velocity in the z-direction).

Sub-regions	*Re*	$\bar{u}_x$(m/s)	$\bar{u}_z$(m/s)
a	**0.014**	2.39E-05	-1.32E-05
	0.029	3.80E-05	-2.10E-05
	0.086	1.02E-04	-5.64E-05
b	**0.014**	2.64E-05	-6.34E-06
	0.029	4.50E-05	-1.15E-05
	0.086	1.17E-04	-3.02E-05
c	**0.014**	4.11E-05	2.36E-08
	0.029	6.95E-05	1.94E-07
	0.086	1.75E-04	5.63E-07
d	**0.014**	2.12E-05	-6.50E-07
	0.029	4.08E-05	-1.40E-06
	0.086	1.07E-04	-4.46E-06
e	**0.014**	9.74E-06	1.15E-06
	0.029	1.70E-05	1.66E-06
	0.086	4.50E-05	4.39E-06
f	**0.014**	1.92E-05	1.46E-06
	0.029	3.00E-05	2.63E-06
	0.043	4.51E-05	4.07E-06
	0.057	5.86E-05	5.16E-06
	0.071	7.19E-05	6.24E-06
	0.086	8.83E-05	7.70E-06
g	**0.014**	1.83E-05	2.13E-06
	0.029	3.61E-05	4.72E-06
	0.086	1.02E-04	1.41E-05
h	**0.014**	3.15E-05	-3.77E-06
	0.029	6.12E-05	-8.37E-06
	0.086	1.67E-04	-2.16E-05

The overestimation rate was estimated for *Re* of 0.014 to 0.086 (Figure 2-8 and Table 2-4) at all the sub-regions. It was -4 to 8 % and 1 to 16 % for smooth-walled subregions c and h, respectively, 36 to 47 % and 19 to 60 % for highly rough-walled subregions e and f, respectively, and 12 to 27 % and 16 to 37 % for moderately rough-walled regions b and g, respectively. Thus, the flow overestimation is caused by the roughness, not inertial forces. The overestimation by the Reynolds equation became larger with roughness (Figure 2-10). Because the magnitude of $\partial^2 u_x / \partial x^2$ and $\partial^2 u_x / \partial z^2$ in the viscous forces grew comparable to that of $\partial^2 u_x / \partial z^2$ with increasing velocity, the average overestimation rate in the eight observed subregions was calculated as 14% at *Re* =0.014, 26% at *Re* = 0.029, and 33% at *Re* = 0.086. This analysis demonstrates that even for low *Re* (< 0.1), the Reynolds equation is valid only at nearly parallel-walled fractures and tend to overestimate the flow rate even at moderately rough-walled regions.

In the 2-D fracture, the forced flow through small aperture zones leads to higher velocity than in the 3-D fracture, where preferential flow is generated through the large aperture region. Subregion c and h with a small aperture but little variation in the roughness show a much smaller overestimation rate than other subregions, a, e, f, and g, with larger apertures and variable roughness, where overestimation occurred even at low *Re*. Thus, this issue is does not fundamentally diminish the findings of this study that roughness plays an important role in the degree of overestimation rather than the aperture size at low *Re*.

Table 2-4 Ratio of viscous force terms $((\partial^2 u_x / \partial z^2)/(\partial^2 u_x / \partial x^2))$ and overestimation ration by equation (2-18)

Sub-regions	Reynolds number	Ratio of viscous forces ()	Overestimation (%)
a	**0.014**	0.477	26.5
	0.029	0.479	36.0
	0.086	0.568	38.7
b	**0.014**	0.328	11.6
	0.029	0.317	19.8
	0.086	0.454	27.3
c	**0.014**	0.173	-3.9
	0.029	0.202	8.3
	0.086	0.242	6.1
d	**0.014**	0.296	8.4
	0.029	0.342	22.3
	0.086	0.485	30.5
e	**0.014**	0.572	36.0
	0.029	0.532	41.3
	0.086	0.646	46.6
f	**0.014**	0.402	19.0
	0.029	0.455	33.6
	0.043	0.617	48.1
	0.057	0.557	41.2
	0.071	0.641	49.7
	0.086	0.784	60.3
g	**0.014**	0.373	16.1
	0.029	0.459	34.0
	0.086	0.549	36.8
h	**0.014**	0.221	0.9
	0.029	0.266	14.7
	0.086	0.338	15.7

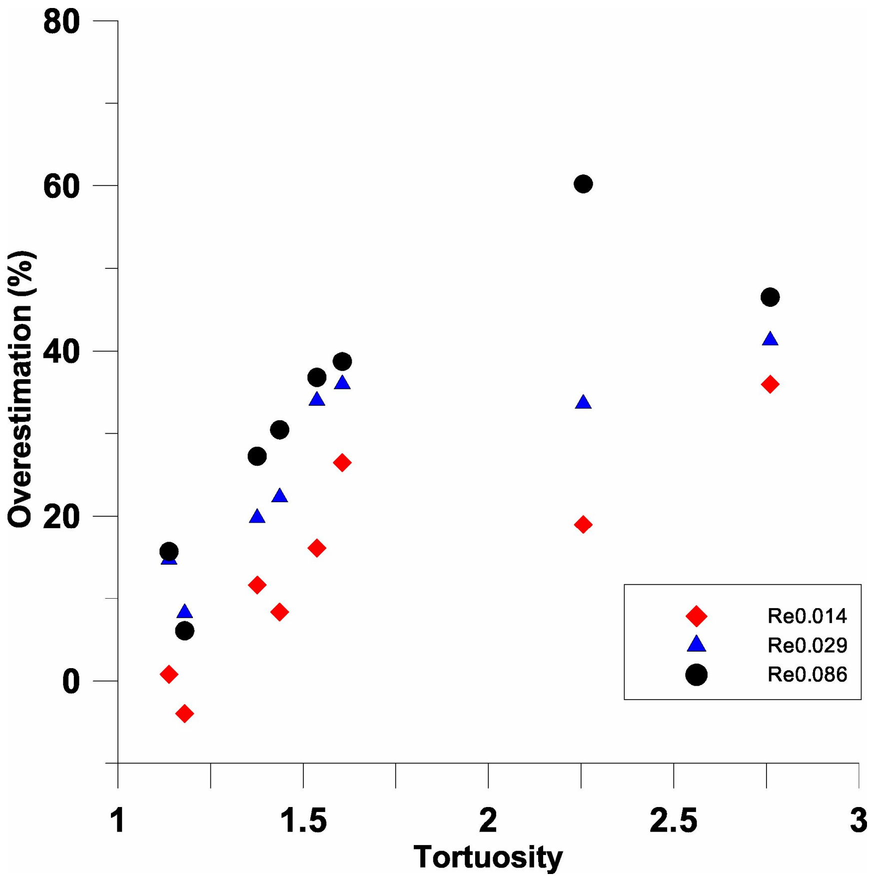

Figure 2-10 Relationship between predicted overestimation (%), tortuosity, and Reynolds number.

2.5 Conclusions

It is generally agreed that as long as the Reynolds number is below 1, then the Reynolds equation rarely overestimates the fluid flow. At the same time, the validity of the Reynolds equation has been questioned because of its overestimation of flow rate even at low *Re* (< 1). The main causes are attributed to nonlinearity by inertial forces and/or abruptly varying apertures. Nonlinearity is also related to the validity of the Stokes equations that are based on a linear flow regime. In this study, the first direct measurement of flow velocity in the parallel- and rough-walled fractures using micro - PIV was made to assess the validity of the Stokes and the Reynolds equations.

Measured velocity vectors were used for the magnitude analysis of inertial and viscous force terms. The analysis showed that inertial forces were much smaller than viscous forces even in the highly rough-walled region for *Re* < 0.1, indicating that nonlinearity is not a cause of the overestimation. Further visual observation of the generation of a recirculation zone about *Re* = ~ 8.6 indicates that the nonlinear flow hardly occurs for *Re* < 1 and the Stokes equations is valid, regardless of fracture roughness.

The Reynolds equation is based on the assumption that $\partial^2 u_x / \partial z^2$ of viscous forces should be a dominant term over $\partial^2 u_x / \partial x^2$. The viscous terms were evaluated with measured velocity vectors at various roughness conditions for $Re < 0.1$. The assumption was not satisfied at rough-walled regions, where the magnitude of $\partial^2 u_x / \partial x^2$ was comparable to that of $\partial^2 u_x / \partial z^2$. It became evident with increasing roughness, which indicates that abrupt aperture change is a main cause of the overestimation at low $Re < 1$.

Further analysis was also conducted to quantify the overestimation by the Reynolds equation. The estimated overestimation became large with increasing roughness and was as high as 47 - 60 % at highly rough-walled regions. The Reynolds equation overestimated the flow rate even at moderate roughness regions for low Re (< 0.1). It was found that a little roughness change in the fracture makes the Reynolds equation overestimate the flow through the fractures even for $Re < 1$.

CHAPTER 3. VISUALIZATION OF SOLUTE TRANSPORT

Tail shortening with developing eddies in a rough-walled rock fracture

CHAPTER 3. VISUALIZATION OF SOLUTE TRANSPORT:

Tail shortening with developing eddies in a rough-walled rock fracture

In this chapter, solute transport characteristics in a single rough-walled fracture were investigated. Breakthrough curves (BTCs) were plotted from the series of experiments to quantify solute dispersion. Based on the dispersion coefficient changes and eddy growths with an increased Reynolds number, the role of eddy flows on solute transport (e.g. tail shortening, Non - Fickian tailing) was analyzed. The experimentally visualized phenomena were confirmed with the aid of numerical simulations based on N-S equation: 2-D simulation at identical conditions from the experiment, and the simulations on idealized, simple 3-D fracture.

3.1 Introduction

Non-Fickian tailings in fracture flow

Accurate estimation of travel and residence times of solutes in fractured rock masses is important for risk assessment of geologic storage of radioactive waste and CO_2 and for cleanup and monitoring strategies for contaminated sites. Field tracer tests, conducted in rock fractures, often exhibit long tails in breakthrough curves, which deviates from Fickian dispersion predictions [*Raven et al.,* 1988; *Becker and Shapiro, 2000]. Qian et al.* [2011] showed that long tails were observed under non-Darcian flow regimes in a sand-filled single fracture.

Non-Fickian tailing has been attributed to (1) diffusive mass transfer between the fracture and the matrix [*Neretnieks,* 1983; *Novakowski et al.,* 1995; *Lapcevic* et al., 1999; *Zhou et al.,* 2006], (2) advective processes within the fracture such as channeling or tortuous flow due to variable apertures [*Neretnieks,* 1983, *Moreno et al.,* 1985; *Tsang and Tsang,* 1987*, Roux et al.,* 1998] and trapping of solutes in immobile (or stagnation) zones near the fracture walls [*Boutt et al.,* 2006; *Cardenas et al.,* 2007, 2009], or (3) sorption of solutes on the fracture walls [Neretnieks et al., 1982].

Unlike the other causes of heavy tailing mentioned above, until recently, the role of immobile fluid zones within the fracture on heavy tailing was mostly speculative. This is because these immobile zones and their interaction with mobile zones were impossible to observe in microscopic rough-walled fractures.

However, the recent development of numerical techniques has enabled the simulation of fluid flow and solute transport in a microscopic rough-walled fracture by directly solving the Navier-Stokes equations [*Boutt et al.*, 2006; *Cardenas et al.*, 2007; *Koyama et al.*, 2008; *Bouquain et al.,* 2012; *Qian et al.,* 2012; *Bolster et al.,* 2014] (Figure 3-1). These studies revealed that eddies develop in regions with abrupt change in aperture and enlarge with increasing fluid velocity, which results in predicted breakthrough curves with heavy tails. However, the fracture geometries for these computational studies all consisted of two-dimensional (2-D) rough-walled fractures. In 2-D fractures, the apertures do not change in the direction perpendicular to the flow direction. This differs significantly from real fractures, which have three-dimensional (3-D) void spaces.

In real 3-D fractures, it is well established that surface roughness leads to variations in fracture aperture in all directions so that large- aperture regions tend to be isolated [e. g., *Keller,* 1998; *Karpyn et al.,* 2009; *Lee et al.,* 2010], resulting in a complex 3-D velocity field in these regions. Therefore, the role of associated eddies on observations of non-Fickian transport needs to be thoroughly investigated in the context of the 3-D nature of rough-walled rock fractures.

Our previous work succeeded in directly observing microscopic flow phenomana occurring in a rough-walled fracture with a micro Particle Image Velocimetry (microPIV) system [*Lee et al.,* 2014]. Here we present the first attempt to directly measure the influence of the flow characteristics between the walls of a rough-walled fracture on solute transport which is used to quantify the onset of eddies and their effect on non-Fickian tailing under flows ranging from Reynolds number (*Re*) of 0.08 to 17.13, where local eddies becomes fully developed. In addition, we present numerical analysis that provides insight into the role of local eddies on fluid flow and transport in 3-D rough-walled fractures

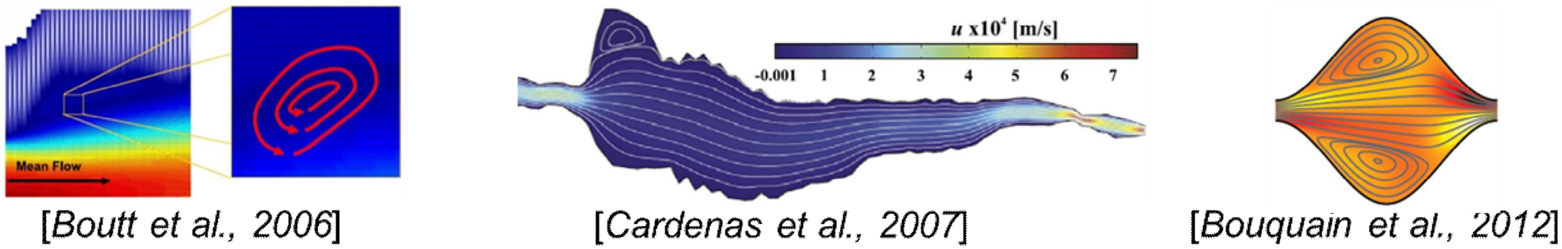

Figure 3-1 Numerically visualized eddies in previous research based on 2-D Navier-Stokes flow simulation.

Relationship between hydrodynamic dispersion and Peclet number

The influence of fracture roughness on a relationship between hydrodynamic dispersion coefficient and average fluid velocity has been studied [*Dronfield and Silliman*, 1993; *Ippolito et al.* 1994; *Roux et al.* 1998; *Keller et al*., 1999; *Detwiler et al.,* 2000]. *Detwiler et al.* [2000] developed the analytical expression between dispersion coefficient and the Peclet number, and showed that dominant dispersion mechanisms highly depends on the Peclet number (proportional to fluid velocity).

Especially, relationship between dispersion coefficient (*D*), and Peclet number (*Pe*) in a single fracture has been reported in the previous researches as $D \propto Pe^{1.04}$ [*Keller et al*., 1999], $D \propto Pe^{1.1}$ [*Keller et al*.,1995], $D \propto Pe^{1.4\sim}$ [*Dronfield and Silliman*, 1993]. According to the studies, the dispersion of solutes in a variable-aperture fracture was affected by the combination of the molecular diffusion, wall-roughness (macro dispersion) and parabolic velocity distribution (Taylor dispersion) (Figure 3-2).

$$\frac{D_L}{D_m} = \tau + \alpha_{macro} Pe + \alpha_{Taylor} Pe^2 \qquad (3\text{-}1)$$

where D_L is dispersion coefficient, D_m is diffusion coefficient, τ is tortuosity, α_{macro} is coefficient for the contributions of macrodispersion, α_{Taylor} is coefficient for the contributions of Taylor dispersion and Pe is peclet number.

Ippolito et al. [1994], *Roux et al*. [1998] and *Detwiler et al.* [2000] suggest that D_L can be expressed as sum of the three components using equation (3-1).

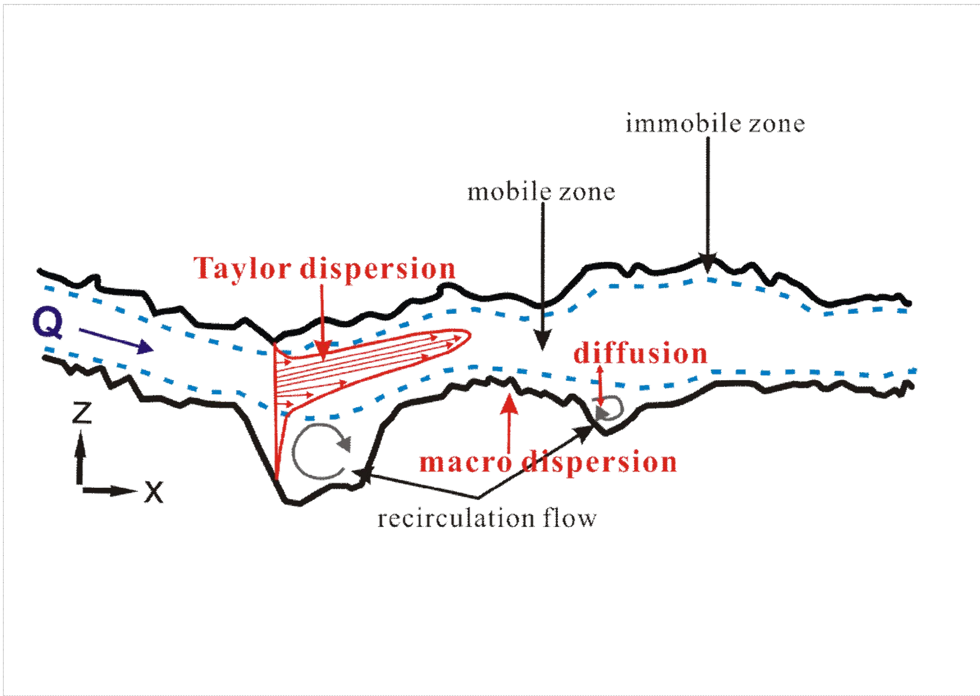

Figure 3-2 Solute transport mechanisms (molecular diffusion, macro dispersion, and Taylor dispersion) in a single rough-walled fracture.

3.2 Methodology

Experiment

Our micro-PIV system enables direct measurement of fluid flow and solute transport in microscopic rough-walled fractures. The system consists of an inverted microscope (Olympus IX-50), syringe pump, CCD camera, mercury lamp, and computer (Figure 3-3). The fracture was prepared by scanning both surfaces of a rough-walled fracture and engraving them on acrylics using the computer numerical control drilling machine resulting in a 200 mm long × 1 mm wide rough-walled fracture. Apertures varied from 387 to 2487 μm with an arithmetic mean aperture and a standard deviation of 1030 μm and 411 μm, respectively (See the Figure 2-3 for more detailed information on the experimental setup).

Fluorescence intensity is linearly proportional to dye concentration in dilute samples [*Lakowicz*, 2006]. For tracer test, Rhodamine B (a fluorescent dye) was diluted with deionized water to achieve a maximum dynamic range (i. e. peak concentration occurred near the sensitivity limit of the light/camera system). Deionized water was injected into the left inlet of the fracture at constant flux to form representative flow conditions at Re = 0.08, 0.29, 2.86, 8.57, and 17.13 ($Re = \rho Ub/\mu$), where U is the macroscopic fluid velocity, calculated by injection flow rate divided by fracture cross-sectional area, i.e., arithmetic mean aperture times fracture width, b is the arithmetic mean aperture, ρ is the water density, and μ is the water viscosity).

As intended flow condition was first established, 5 μL of diluted Rhodamine B (a fluorescent dye) with deionized water was instantaneously injected at the point 1 cm distant from the inlet and filled the fracture fully around the injection point, the flow was restarted for the tracer test. Molecular diffusion coefficient of Rhodamine B (D_m) is 3.6×10^{-10} m^2/s. The corresponding Peclet number ($Pe = Ub/D_m$) was 238, 795, 7948, 23,843, and 47,658 for Re = 0.08, 0.29, 2.86, 8,57, and 17.13, respectively.

During the tracer test, continuous snapshots were captured at two observation points (OP1 and OP2) at time interval (e.g., 16 and 0.08s for Re = 0.08 and 17.13) using a CCD camera (Figure 3-3). We estimated the development length (L) for the fully turbulent flow using $L = 4.4bRe^{1/6}$ [*White,* 2011]. We found the expected development length on the order of 7 mm for the largest Re = 17.13, which was far away from the observation points. This development length was related to a time scale on the order of 0.4s. The fluorescence intensity measured across the fracture aperture (128 pixels) at the observation point was summed (Figure 3-3) to provide a measure of the total fluorescence intensity at each time.

Then, the intensity at each time was normalized by the cumulative intensity, which was calculated by summing up the intensities measured at the observation point over the entire observation time period. The normalized fluorescence intensity at a given time, hereafter called the relative concentration, was used to plot the breakthrough curve (BTC) for each experiment.

Understanding the distribution of velocities within a rough-walled fracture is important for better interpretation of solute transport. The potential formation of eddies within large-aperture regions is particularly important to solute transport. Therefore, we also measured the development of eddies at a representative large-aperture area (OP3) just upstream from OP1 for the same representative *Re* as in the tracer test (Figure 3-3). Deionized water mixed with 1 μm diameter fluorescent particles was injected into the left inlet of the fracture at constant rate. Images acquired at the same frame rate as above yielded flow paths (stream lines) traced out by fluorescent particles moving with the flow.

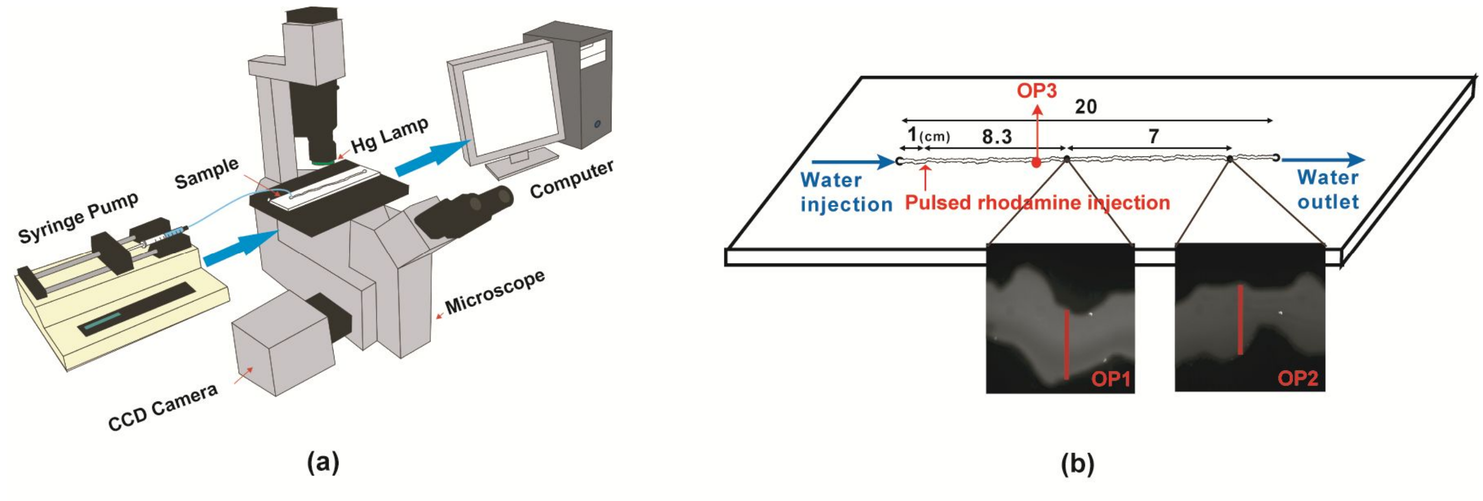

Figure 3-3 Schematic drawings of (a) experimental setup of micro-PIV. (b) Solute are monitored at OP1 and OP2. Flow trajectories are observed at the large-aperture regions located at OP3.

Numerical simulation

Micro-PIV provides a depth-integrated view of fluid flow and solute transport; to complement these measurements and develop a more thorough understanding the 3-D nature of the velocity field, we modeled flow and transport through the experimental geometry using COMSOL Multiphysics, the commercial finite element method software [*COMSOL AB*, 2013]. The single-phase flow of incompressible Newtonian fluid in steady state is governed by the Navier-Stokes equations:

$$\rho(\mathbf{u}\cdot\nabla)\mathbf{u} = \mu\nabla^2\mathbf{u} - \nabla p\,, \tag{3-2}$$

where ρ is the density, g is the gravitational acceleration, **u** is the 3-D velocity vector, μ is the viscosity, and p is total pressure. The Navier-Stokes equations must be supplemented by the continuity equation:

.

$$\nabla\cdot\mathbf{u} = 0 \tag{3-3}$$

The Reynolds number range in our experiment, and in the simulation is limited to 17.1. For a case of simulation based on the Navier-Stokes equation, there is the potential to generate a turbulent flow, representing a time-dependent velocity, which may violate the steady-state assumption. *Zou et al.* [2015] performed transient flow simulations on a single rough-walled fracture with the range of *Re* = 1 to 1000. They showed that the steady state assumption is satisfied in the range of *Re* = 1 to 100. A turbulent flow, evident time-dependent eddy behavior, occurred when *Re* reached nearly 1000. Furthermore, many studies assumed a steady-state flow when simulating a fluid flow in a single rough-walled fracture when the Reynolds number was less than 100, as represented in Table 3-1. Therefore, the steady-state assumption appears to be reasonable when *Re* is less than 100.

The numerically-calculated velocity was then coupled with the advection-diffusion equation for solute transport through the fracture:

$$\frac{\partial C}{\partial t} = D\nabla^2 C + \nabla \cdot \mathbf{u}C \tag{3-4}$$

where C is the solute concentration, t is the time, and D is the molecular diffusion coefficient set at 3.0×10^{-10} m^2/s. The boundary conditions and fracture geometries in the study are graphically summarized in Figure 3-9, and described in Chapter 3.3.2.

Table 3-1 Reynolds number range in previously performed N-S flow simulations in a single rough-walled fracture.

Previous studies	***Reynolds number range***	
This study	0.09 ~ 17.1	
Brush & Thomson, 2003	0.01 ~ <1000	
Cardenas et al., 2007	0.15 ~ 0.98	
Koyama et al., 2008	About 0.1~100	*steady state assumption*
Cardenas et al., 2009	0.01 ~ 100	
Bolster et al., 2014	1 ~ 100	
Zou et al., 2015	~ 1000	*transient simulation*

3.3 Results

3.3.1 Experimental results

Breakthrough curves at observation point

Figure 3-4 shows the variation of the intensity as fluorescent tracer entered and left at OP1 and OP2. As solute entered the observation window, the images became brighter and darker as the tracer plume exited.

The relative concentration measured at OP1 and OP2 was plotted against pore volume (PV) in Figure 3-5. At *Re* = 0.08, the BTCs indicated Fickian transport with no appreciable tails. As the flow rate increased up to *Re* = 2.86, the BTC became increasingly skewed to later times, and the peak arrived earlier and decreased in magnitude. However, as the flow rate increased further, the amount of tailing began to decrease.

At *Re* = 8.57, the tail was still observed, but the tailing decreased and the BTC peak concentration increased. This trend persisted through the largest flow rate (*Re* = 17.13) (Figure 3-5). The same flow rate dependence of the BTC was observed at OP2. The reduced tailing observed at both OP1 and OP2 for the highest flow rates differs from results of previous computational studies, which showed monotonically increased tailing with increasing velocity due to eddies that grow with velocity.

The tail shortening, observed at both OP1 and OP2, is contrary to our understanding from the previous studies that tailing grows stronger with increasing velocity due to eddies that are enlarged with velocity [*Boutt et al.*, 2006; *Cardenas et al.*, 2007; *Koyama et al.*, 2008; *Bouquain et al.,* 2012]. The tracer tests were repeated many times, but produced the same results, which strongly indicates that tail shortening can take place physically in the fracture.

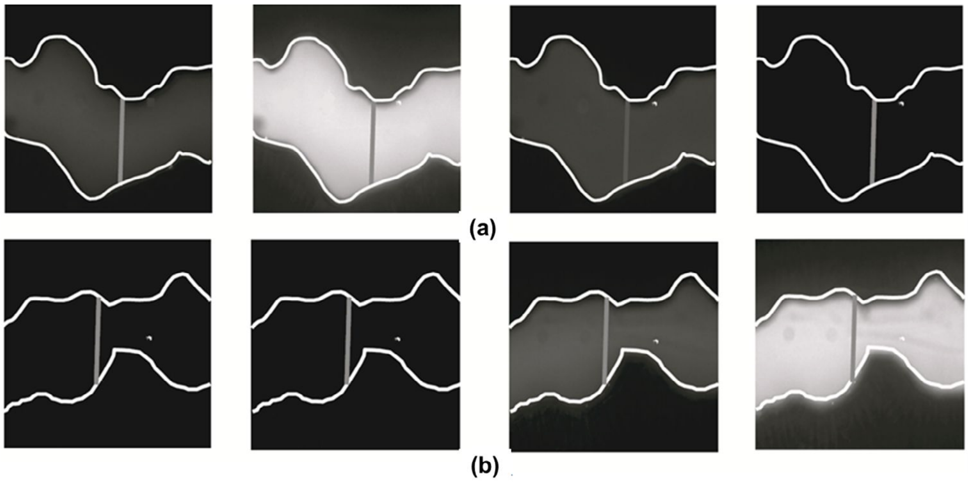

Figure 3-4 (a) Snapshot images showing the intensity variation under 0.4, 0.66, 0.93, and 1.19 pore volume injection at OP1, (b) at OP2.

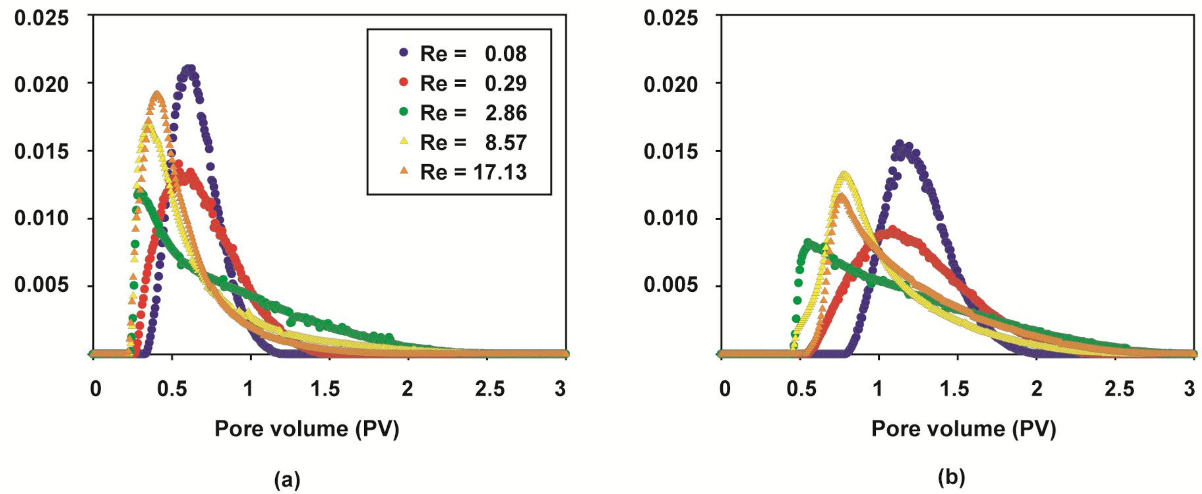

Figure 3-5 The BTCs showing relative concentration at (a) OP1 and (b) OP2 with pore volumes (PVs).

Eddy growth with an increased Reynolds number

Tail shortening observed at higher flow rates at OP1 and OP2 appears to be closely related to characteristics of the flow within the fracture. Figure 3-6 clearly shows the flow paths traced out by fluorescent particles moving with the flow.

At $Re \leq 2.86$, the fluorescent particles moved along parallel layers with no appreciable eddies. Figure 3-6 clearly show much slower velocities near the upper wall of the large aperture area than within the main flow channel as velocity increases. The difference in fluid velocity between the near-wall portion and the main flow channel within the large aperture region grew larger with increasing velocity. These results suggest that the increased tailing observed in the BTCs results from increasing differences in velocities across the fracture width in the absence of eddies.

At $Re = 8.57$, as the particles exited the narrow aperture region, they flowed backward into the near-wall portion of the large-aperture region (Figure 3-6), indicating formation of an eddy. The eddy observed at OP3 is representative of eddies observed in other rapid expansions throughout the fracture. These observations are consistent with previous numerical studies that showed eddies growing in local large-aperture regions with increasing velocity.

However, unlike the previous numerical studies, our experiments showed that particles that entered eddies were relatively quickly cast back into the main flow channel. That is, there was no well-defined separation stream surface delineating so-called immobile (recirculation) and mobile zones as is predicted by purely two- dimensional simulations [*Boutt et al.*, 2006; *Cardenas et al.*, 2007; *Bouquain et al.,* 2012]. This phenomenon became very clear at *Re* = 17.13 (Figure 3-6). The eddies observed at other subregions under the condition of *Re* = 17.13 (Figure 3-7), also indicate that eddies formed in highly aperture variable areas possibly act as advective flow path between mobile zone and immobile zone.

Repeated tests produced the same results, which leads to the hypothesis that three-dimensional effects in the velocity field lead to mass transfer by advective paths connecting eddies and the main flow channel. This mass transfer decreased tailing at large velocities because the residence time in eddies is significantly reduced. However, because our experiments provide a depth-integrated view of the velocity field within the fracture, it is not possible to directly test this hypothesis.

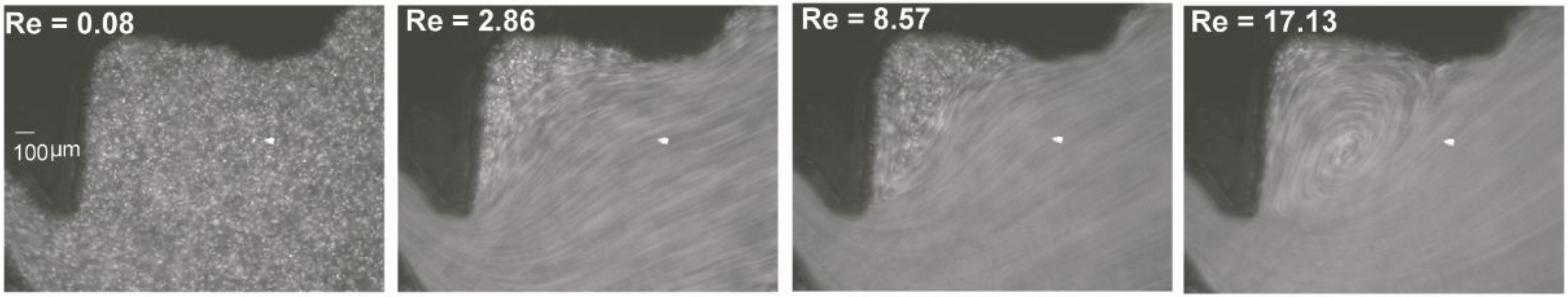

Figure 3-6 Images showing the evolutions of eddies at OP3 with increasing fluid velocity.

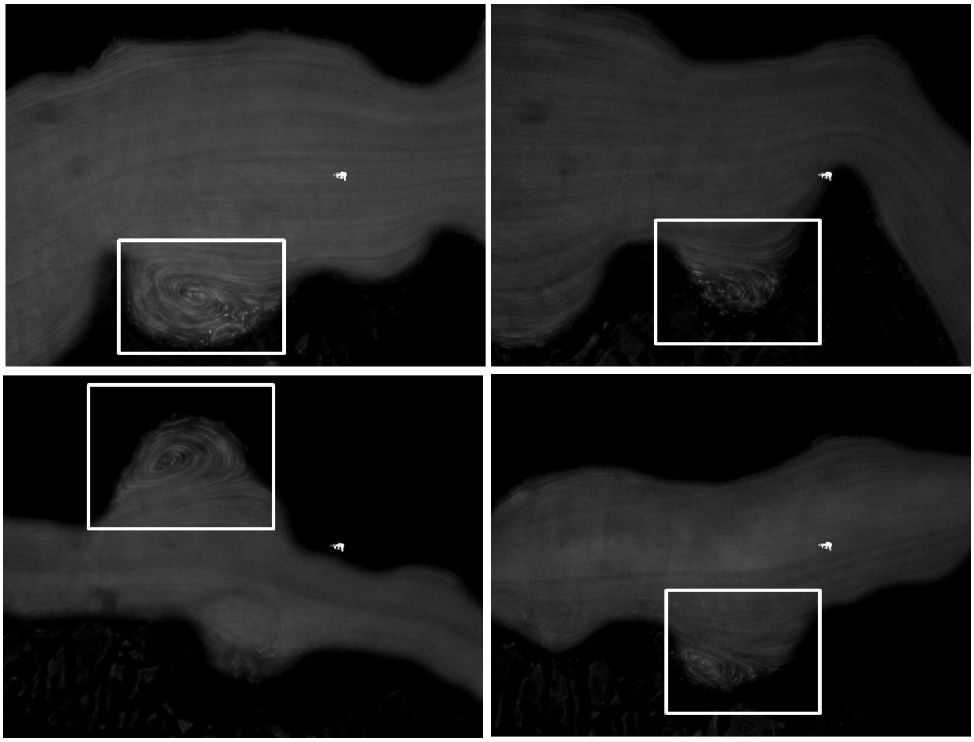

Figure 3-7 Generation of eddies at the highly aperture-variable subregions at $Re = 17.13$.

Estimation of dispersion from experimentally observed BTCs

There are two approaches to estimate dispersion coefficient from breakthrough curves: (1) curve fitting method: dispersion coefficient is determined by minimizing the sum of the squared differences between observed and fitted break-through curves [*Toride et al.,* 1995], and (2) moment method: pore water velocity (v) and dispersion coefficient of the advection-dispersion equation can be directly calculated from following expressions [*Kreft and Zuber*, 1978; *Leij and Dane*, 1991; *Yu et al,* 1999].

According to *Yu et al*. [1999], the normalized moment (M_n) and the nth central moment (μ_n) is represented as:

$$M_n = \frac{m_n}{m_0} = \frac{\int_0^{\infty} t^n C(z,t)dt}{\int_0^{\infty} C(z,t)dt} \tag{3-5}$$

$$\mu_n = \frac{\int_0^{\infty} (t-M_1)^n C(z,t)dt}{\int_0^{\infty} C(z,t)dt} \tag{3-6}$$

where C is the solute concentration, t is the time, m_n is the nth order time moment, μ_n is the nth central moment, z is the distance downward.

From the 1st normalized moment and the 2nd order central moment, pore water velocity (v) and dispersion coefficient (D) is estimated as equation (3-7) and equation (3-8).

$$v = \frac{z}{M_1} \tag{3-7}$$

$$D = \frac{\mu_2 v^3}{2z} \qquad (3\text{-}8)$$

Using the experimentally derived BTCs from the OP1 and the OP2, dispersion coefficients at each condition of Pe are determined as shown in Figure 3-8. According to the Equation (3-1), diffusion mechanism is dominant at low velocity (gradient of Pe versus D_L/D_m in log-log scale: 0), macro dispersion is dominant at the medium velocity (gradient of Pe versus D_L/D_m in log-log scale: 1), and Taylor dispersion is dominant at high velocity (gradient of Pe versus D_L/D_m in log-log scale: 2).

In the results, distinctive pattern was observed at $Re > 2.87$ compared to the pattern at $Re < 2.87$. In the case of $Re < 2.87$, D was proportional to the power of 1.53 of the velocity, which can be explained by the combination of the macro dispersion and Taylor dispersion. On the other hand, D was proportional to the power of 0.79 of velocity in the case of $Re > 2.87$.

The theoretical curves were compared to the estimated D which was derived from the BTCs based on moment method approach. The curves show that dispersion coefficient should converge to the Tayler dispersion with an increased velocity. However, there are some deviations over the $Pe > 10^4$, suspecting whether the theoretical curves satisfy the experimental results in a highly rough-walled fracture. The graph clearly shows the deviation start to occur after Pe around eddy generation in the experiment.

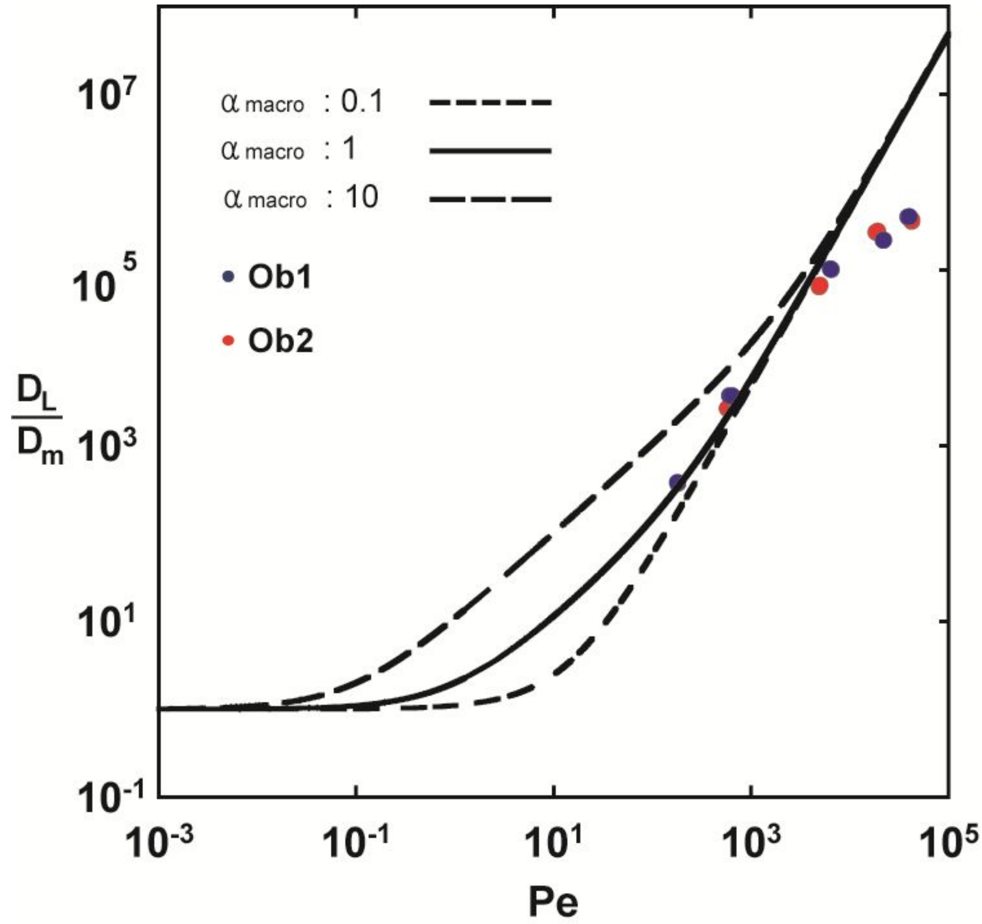

Figure 3-8 D_L/D_m against *Pe* (Comparison of the theoretical curves from equation (3-1), and estimated *D* from the series of experiment).

3.3.2 Numerical simulation results.

Numerical study, using COMSOL Multiphysics, was carried out to assess the cause of tail shortening by mass transfer by advective paths connecting eddies to the main flow channel. Firstly, flow and transport simulations on 2-D domain which is identical to experimental condition are conducted. Secondly, flow simulation on local 3-D domain at the OP3 is carried out to identify advective flow paths in the condition of 1mm depth. Finally, idealized 3-D model including large-aperture area was constructed. In the model, solute BTCs with an increased velocity was analyzed to investigate the relationship of tail shortening and eddy generation in detail.

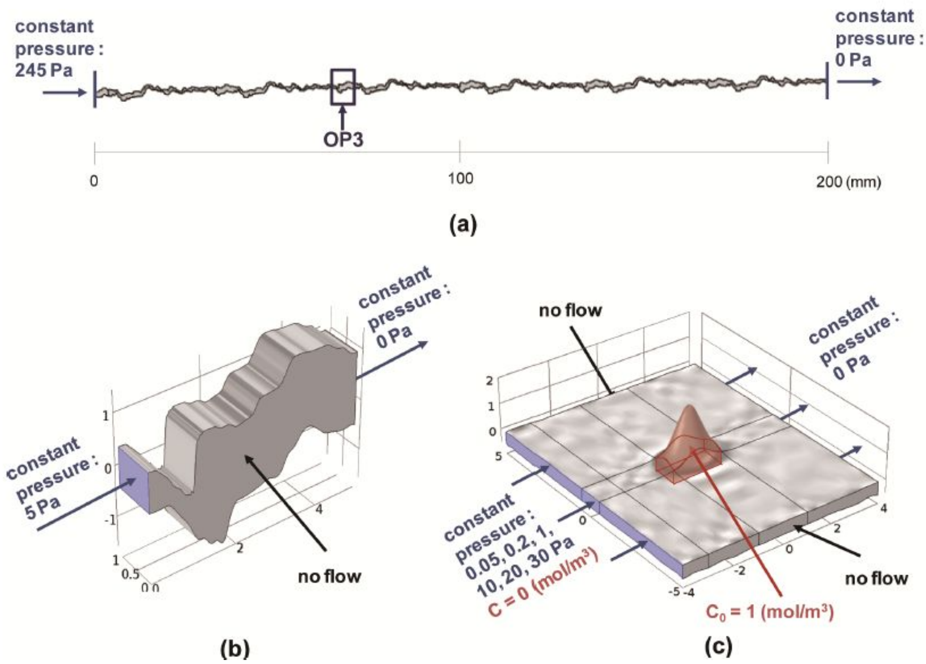

Figure 3-9 The boundary and initial conditions used for numerical modellings: (a) for 2-D simulations, (b) for local 3-D simulation at OP3, and (c) for 3-D simulations for idealized 3-D model.

2-D simulations

As shown in Figure 3-9a, the 2-D domain of fracture was constructed, which is same size of the sample in the experiment. The flow conditions with *Re* = 0.08, 0.29, 2.86, 8.57, and 17.13 (pressure drop conditions at each Reynolds number were summarized in Table 3-1) were simulated.

Constant pressure boundary conditions were set for the left (upstream) and the right (downstream) boundary. And, no flow conditions were set at the upper and at the lower walls of the fracture (Figure 3-10). At each pressure drop condition, steady flow simulations were conducted. Through the flow simulations, velocity fields were determined over the whole 2-D fracture domain. The velocity vectors were coupled with the advection-diffusion equation (equation 3-4), which enabled to the transient solute transport simulations. Through the transient simulations, time series of solute concentrations over the whole 2-D fracture were determined. The concentration changes as injected pore volume at OP1 and OP2 were used to plot the BTCs from the numerical simulations. The information of mesh construction, initial condition, boundary condition, and procedure of 2-D simulations were summarized in the Figure 3-10.

The BTCs from the simulations showed that Fickian distribution under low velocity. In the simulations, consistent changes to non-Fickian tailing distribution with an increased velocity were observed even after the generation of eddies (Figure 3-11). These simulation results are consistent with the previous numerical studies. The trajectories of eddies from the 2-D simulations were represented as recirculation zone (immobile zone), indicating no advective flow paths were generated between eddies and main flow channel.

The recirculation zones near the upper and lower walls of the large-aperture region, shown in the 2-D simulation, remained disconnected from the main flow channel. Although the sizes of eddies were similar between the 2-D simulation and the experiment, the trajectory of eddies were connected to main flow channel in the experiment (Figure 3-12).

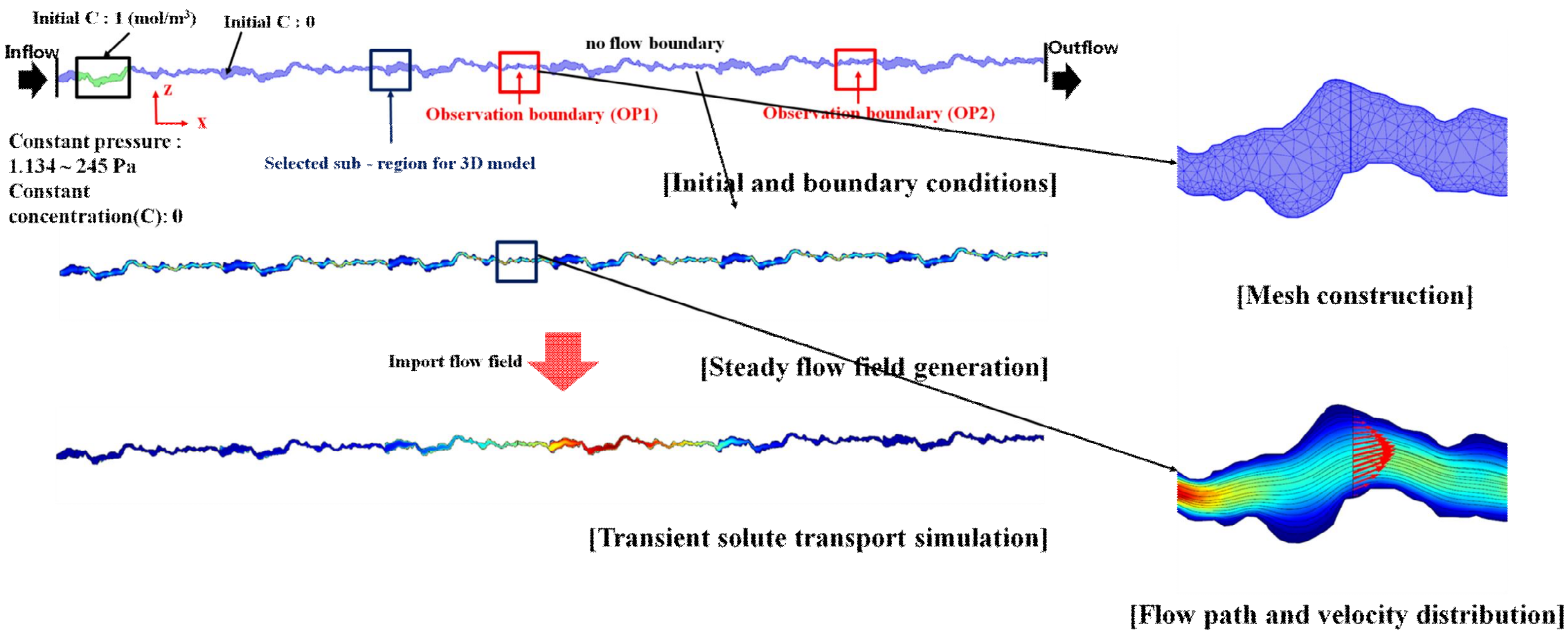

Figure 3-10 Mesh construction, initial, and boundary conditions for 2-D simulations.

Table 3-2 Pressure differences between inlet and outlet for obtaining the same Reynolds number conditions of 2-D experiment.

Pressure difference (ΔP)(Pa)	**Reynolds number (*Re*)**
1.134	**0.08**
3.78	**0.29**
38	**2.86**
117	**8.57**
245	**17.13**

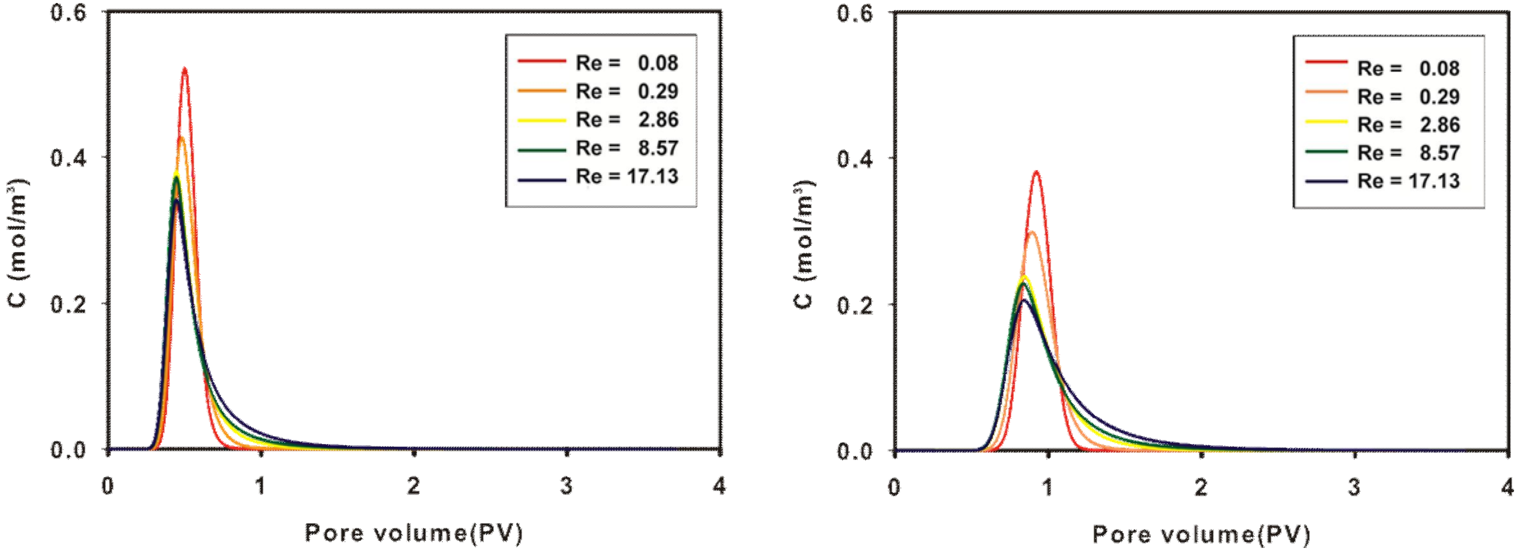

Figure 3-11 The BTCs showing relative concentration at (a) OP1 and (b) OP2 with pore volumes (PVs) from the 2-D simulations.

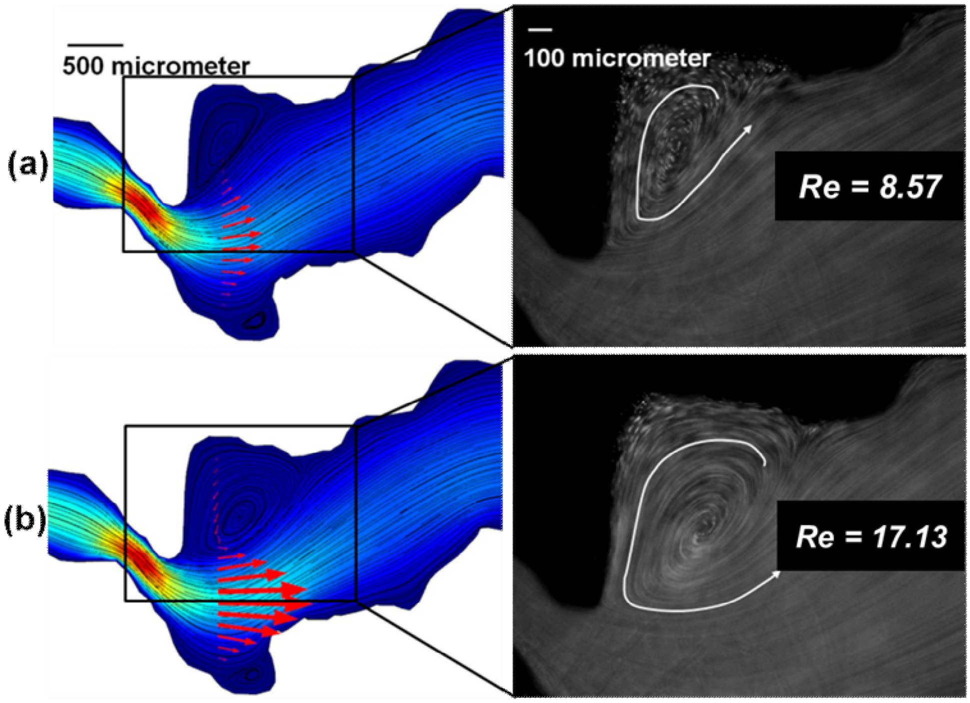

Figure 3-12 Comparison between the flow path from the 2-D N-S flow simulation results (left) and that from the experiments (right) (a) *Re* = 8.57, (b) *Re* = 17.13.

Local 3-D simulation at OP3

To test whether 3-D effects may be responsible for mass transfer by advective paths from eddy to main flow channel, which was observed in the experiments, we extended the 2-D model to 3-D. For the 3-D modeling, the fracture was extended into 3-D with the width of 1 mm (i.e., the y axis in Figure 3-9b). Flow with Re = 19.29 (pressure drop of 5 Pa) was simulated between the upstream and downstream. Constant pressure boundaries with no-flow condition set at the upper and lower walls (Figure 3-9b). The front and rear lateral boundaries (the faces normal to the y axis) were also no-flow boundaries.

This boundary condition represents the experimental conditions during our tracer and flow tests, whereas for 2-D simulations (Figure 3-13a), the fracture is implicitly assumed to be infinite in the y direction. The results showed a clear 3-D trajectory of streamlines in the 3-D simulations. Flow trajectories swirled around the upper and lower near-wall portions of the large- aperture region and reentered the main flow channel (Figure 3-13c and 3-13d), which agreed very well with our observation shown in Figure 3-6. The numerical studies suggest that 3-D effects resulting from introduction of no- flow lateral boundaries significantly enhance mass transfer by advective paths connecting eddies to the main flow channel. It is reasonable to expect that this mass transfer will cause shortening of the heavy tails as eddies are developed at larger Re.

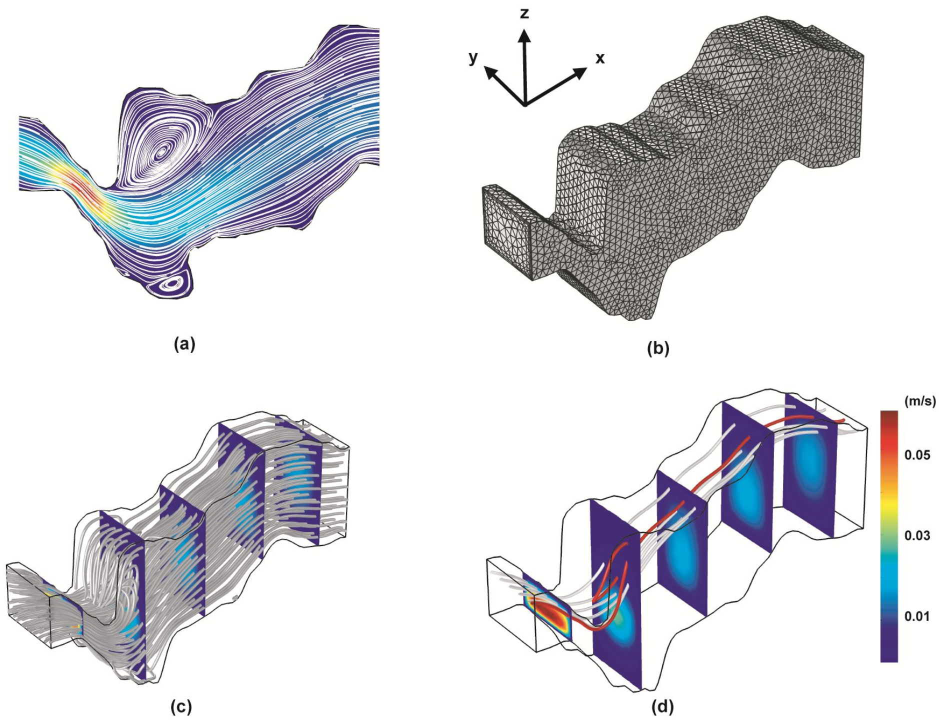

Figure 3-13 Numerical results showing the flow characteristics between the recirculation zone and the main flow channel in (a) 2-D and (b) 3-D fracture geometries. The 3-D fracture has the front and rear lateral boundaries (the faces normal to the y axis are set at no flow), whereas the 2-D fracture is infinite. (c) The flow trajectories near the walls of the large-aperture region and (d) the clear view of the flow trajectories shown in Figure 3-13c.

3-D simulation at idealized 3-D model

Our experimental and computational results, in a fairly simple essentially 2-D flow geometry, suggest that 3-D effects caused by aperture expansions are likely significant in transport through more realistic 3-D fractures. To test this, we simulated flow through a simple 3-D fracture.

As mentioned in the introduction, in real fractures the aperture tends to vary in all directions. We developed an idealized 8 × 10 mm, 3-D fracture that includes a single large-aperture region as shown in Figure 3-14a. The large-aperture region has an arithmetic mean and maximum aperture of 1.28 mm and 2.43 mm, respectively, and the surrounding relatively uniform apertures (i.e., not constant but slightly varying) has an arithmetic mean of 0.5 mm. The 3-D flow field was meshed with 212,711 tetrahedral elements with mesh refinement in the large-aperture region to minimize numerical dispersion.

A constant pressure drop (ΔP) between the left upstream and right downstream boundaries was imposed at 0.05 (Re = 0.06), 0.2 (Re = 0.22), 1 (Re = 1.10), 10 (Re = 10.92), 20 (Re = 21.36), and 30 Pa (Re = 31.31). The front and rear lateral boundaries were set at no flow (Figure 3-9c).

For pressure drops less than 10 Pa, no remarkable change in streamlines was observed (Figure 3-15). At ΔP = 10 Pa, the low velocity zone near fracture surface in the large-aperture region with no indication of eddy formation. A closer examination of the trajectories (by increasing trajectory density) revealed that small incipient eddies occurred near the upper wall. At ΔP = 20 Pa and 30 Pa, these eddies became fully developed and the advective paths from inside the eddy to the main flow channel were clearly evident (Figure 3-14b and Figure 3-15).

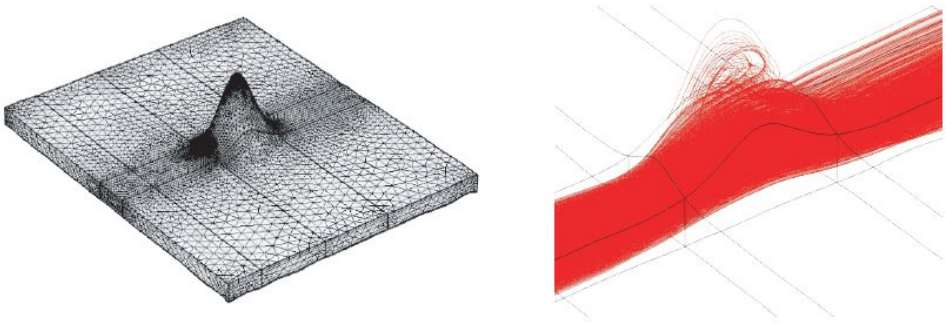

(a) (b)

Figure 3-14 (a) Numerical setup for the fracture with a large-aperture region and the surrounding relatively uniform aperture (b) The fluid flow trajectories at ΔP = 20 Pa.

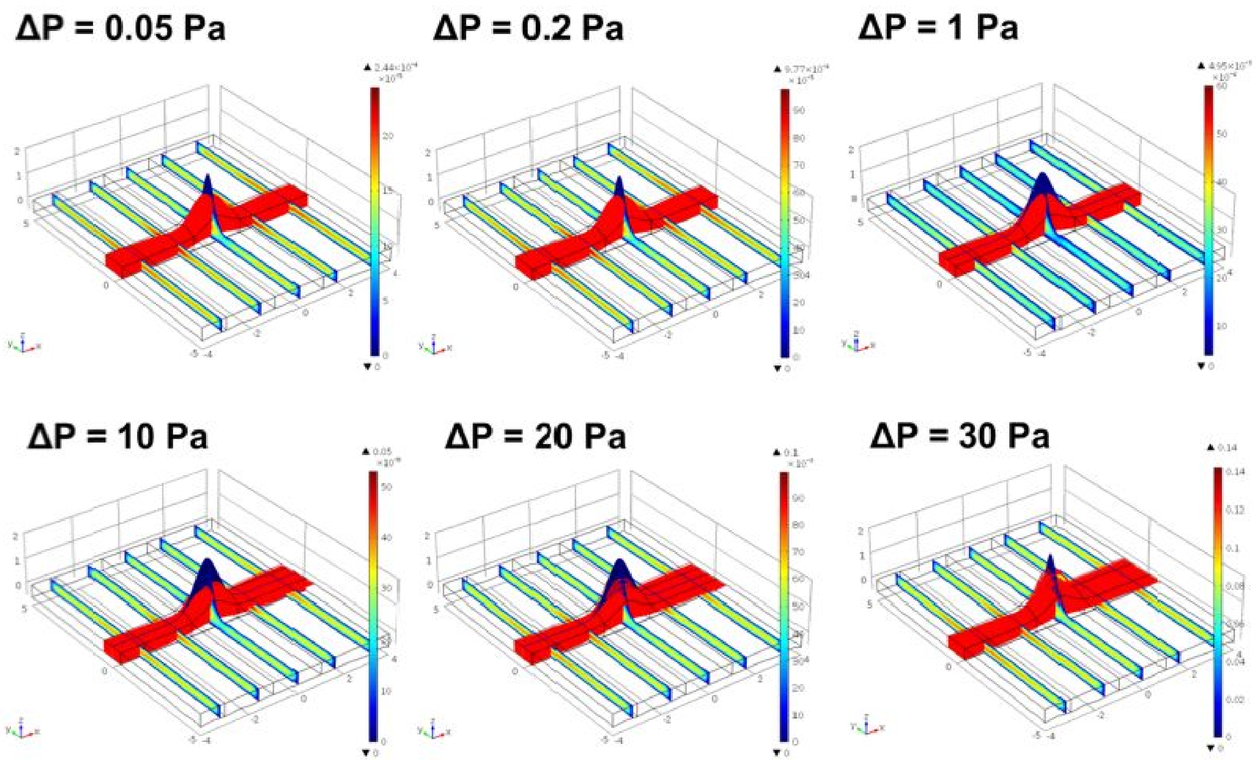

Figure 3-15 The fluid velocity distribution and trajectories at pressure drops of 0.05, 0.2, 1, 10, 20, and 30 Pa.

Further numerical modeling was conducted to assess the amount of mass transfer by advective paths connecting the inside eddy to the main flow channel. Initially, the larger-aperture region was filled with solute at a concentration of C_0 = 1 mol/m^3; the initial concentration elsewhere in the fracture was C_0 = 0 mol/m^3. For the transport simulations, the flow boundary conditions were as described in the previous paragraph (Figure 3-9c). The corresponding Pe was 1.84×10^2, 7.36×10^2, 3.67×10^3 3.65×10^4, 7.13×10^4, and 1.05×10^5 for ΔP = 0.05, 0.2, 1, 10, 20, and 30 Pa, respectively.

Figure 3-16 is the summarized residual solutes changes in a large aperture area, representing remarkable residual changes with respect to the pressure drop conditions of 0.05, 10, and 30 Pa. The pressure drop conditions are representative velocity conditions for no eddy, weak eddy, and fully developed eddies, respectively. The results show the increased amount of residual solutes until the ΔP = 10 Pa (Figure 3-16b), which was reduced with an increase of velocity (ΔP = 30 Pa) (Figure 3-16c).

Temporal changes of the residual concentration distributions at initial, 3PVs, 10PVs, 30PVs for all pressure drop conditions are represented (from Figure 3-17 to Figure 3-22). More solute remained in the large-apeture region after equal number of PVs as fluid velocity increased up to ΔP = 10 Pa (Figure 3-17 to Figure 3-20), indicating the development from Fickian to non-Fickian transport. At ΔP = 10 Pa, some solute was flushed from the large-aperture region due to mass transfer by advective paths from the eddy to the main flow channel, which became pronounced at ΔP = 20 Pa. As the eddy was fully developed at ΔP = 20 Pa and 30 Pa, the solute was more readily flushed from the large- aperture region such that less solute remained in the large- aperture region (Figure 3-21 and Figure 3-22). This observation of enhanced flushing within an eddy is consistent with our experimental observations that showed reduced tailing as flow rate increased.

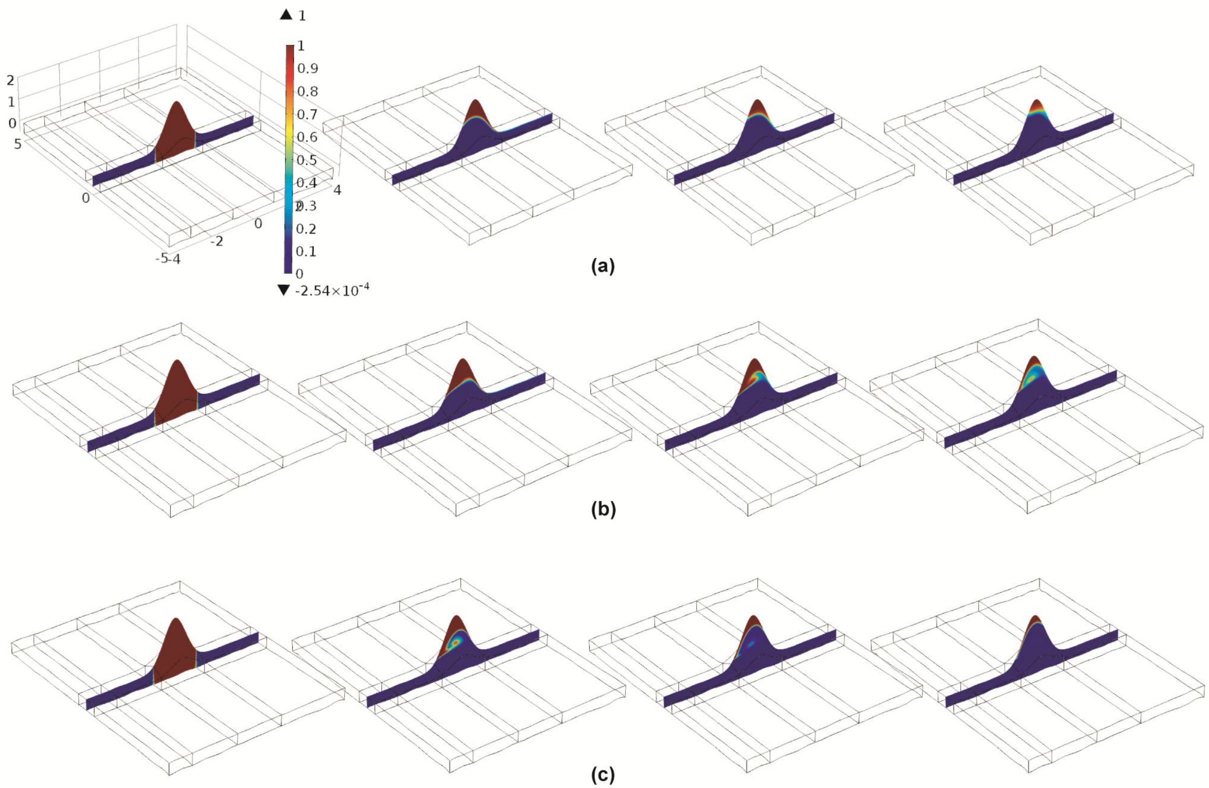

Figure 3-16 The residual concentrations at the large-aperture area at (a) PV = 0, 3, 10, and 30 when ΔP = 0.05 Pa, (b) PV = 0, 3, 10, and 30 when ΔP = 10 Pa (c) PV = 0, 3, 10, and 30 when ΔP = 30 Pa.

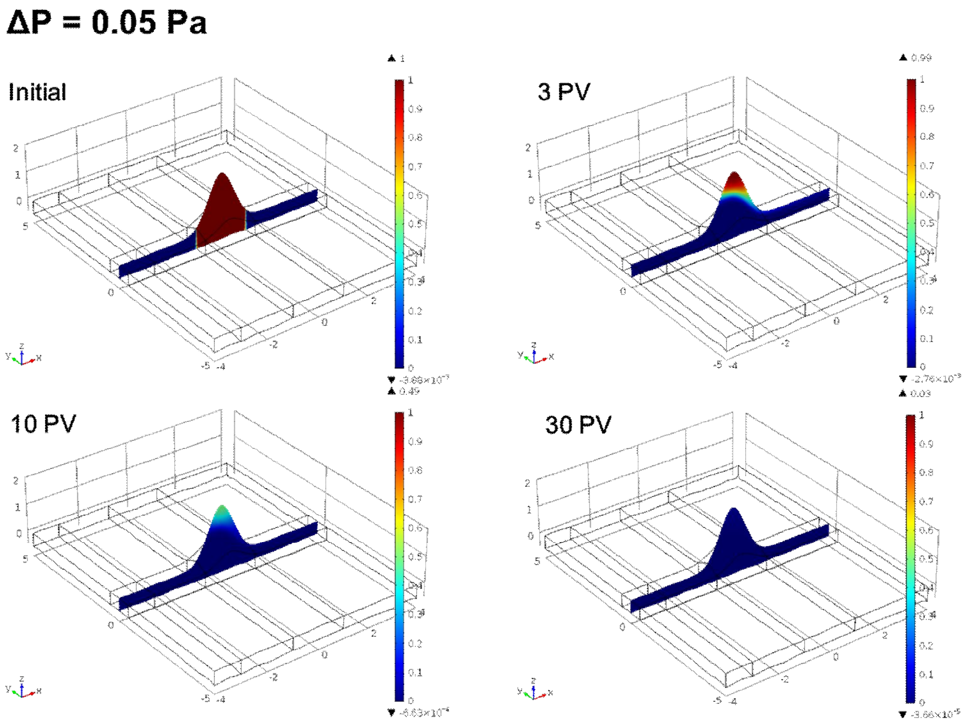

Figure 3-17 Solutes initially set at the large aperture area, and the residual concentration at PV = 3, 10, and 30 when $\varDelta P$ = 0.05 Pa.

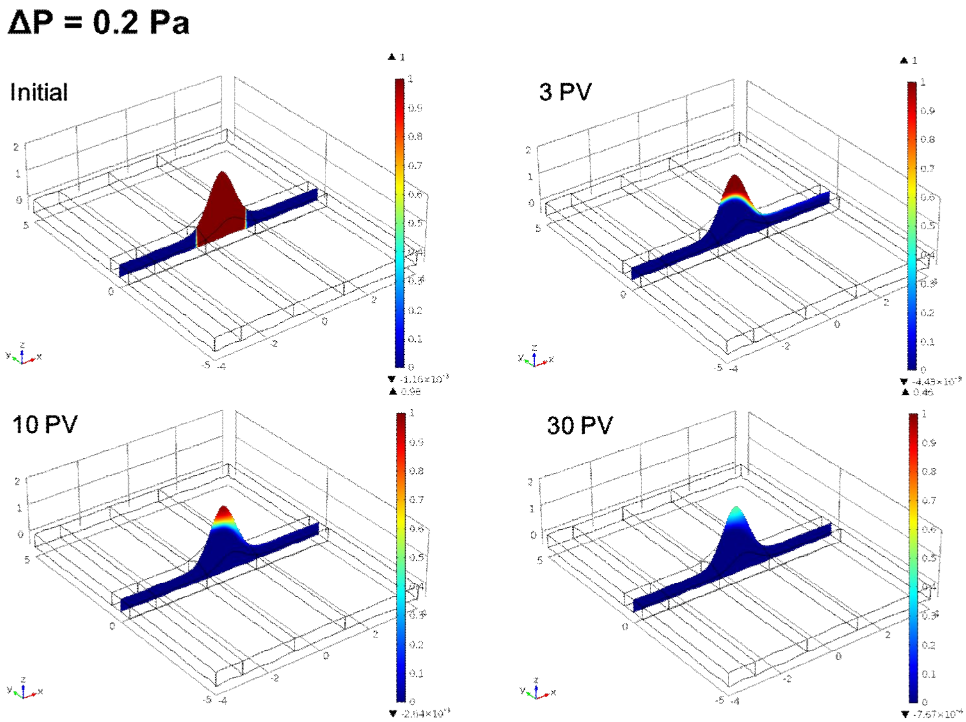

Figure 3-18 Solutes initially set at the large aperture area, and the residual concentration at PV = 3, 10, and 30 when ΔP = 0.2 Pa.

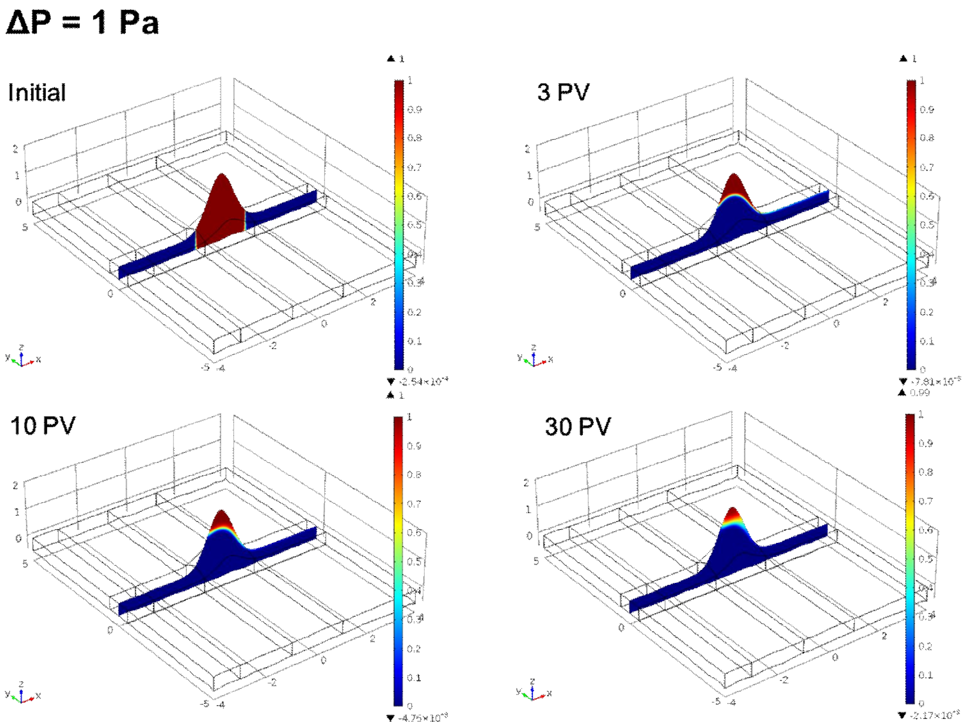

Figure 3-19 Solutes initially set at the large aperture area, and the residual concentration at PV = 3, 10, and 30 when ΔP = 1 Pa.

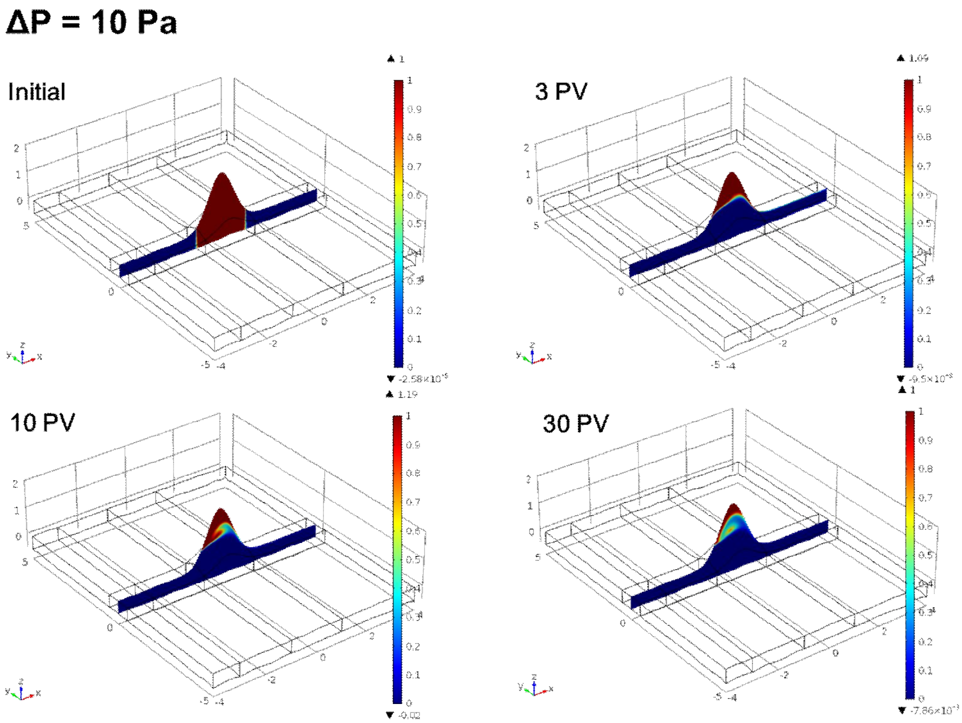

Figure 3-20 Solutes initially set at the large aperture area, and the residual concentration at PV = 3, 10, and 30 when ΔP = 10 Pa.

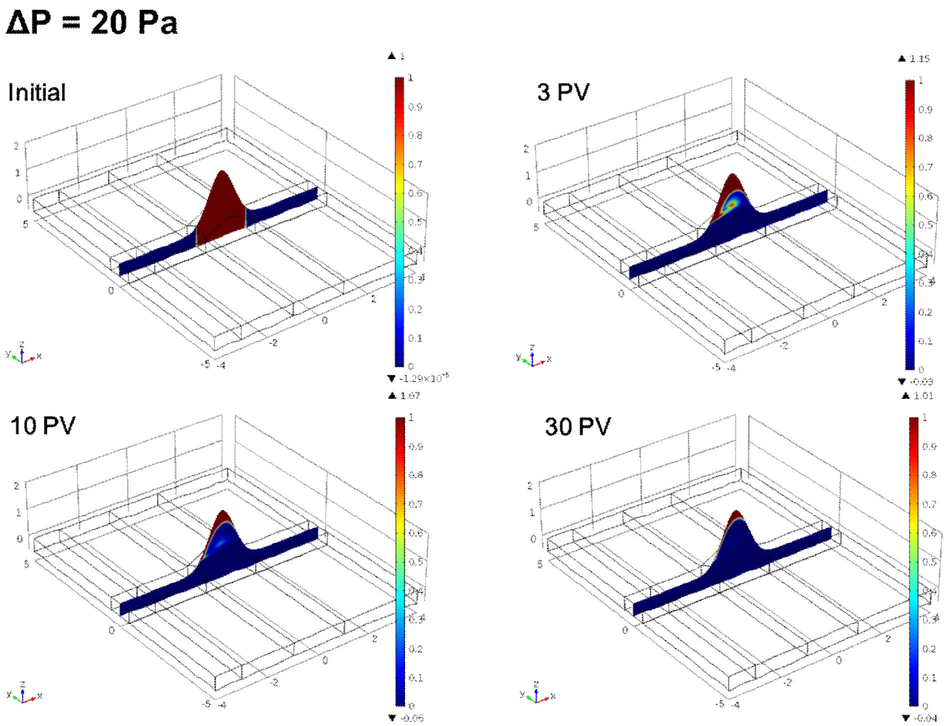

Figure 3-21 Solutes initially set at the large aperture area, and the residual concentration at PV = 3, 10, and 30 when ΔP = 20 Pa.

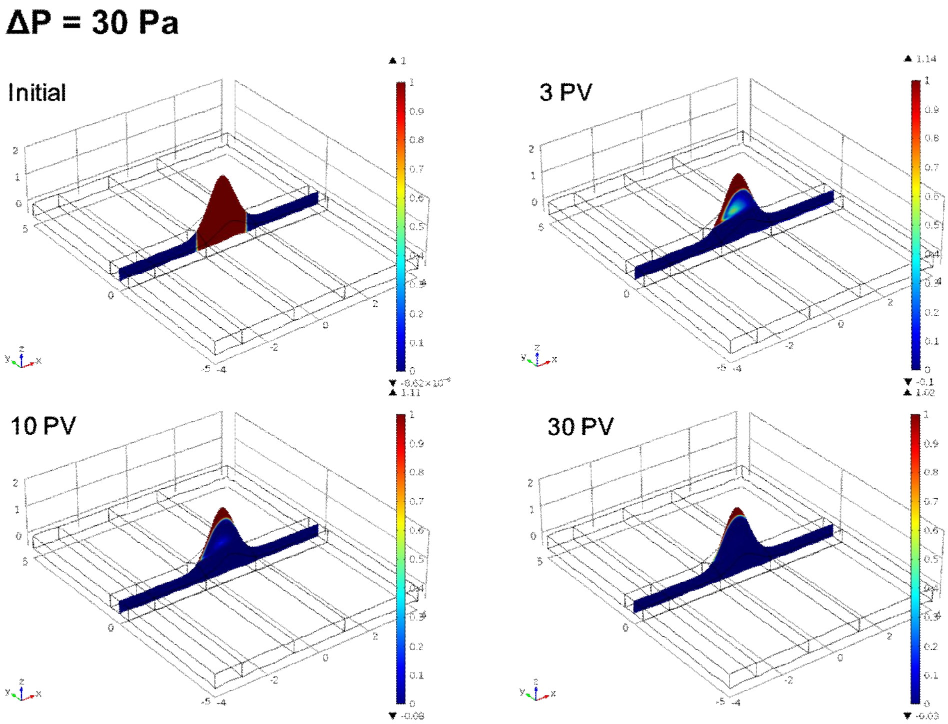

Figure 3-22 Solutes initially set at the large aperture area, and the residual concentration at PV = 3, 10, and 30 when ΔP = 30 Pa.

Figure 3-23 shows the mean concentration within the large-aperture regions plotted against pore volumes. The concentration time series show that the most significant tailing occurred at ΔP = 10 Pa. At larger flow rates, the tails began to decrease. Our numerical simulation support the hypothesis that 3-D flow effects in the vicinity of large expansions in fracture aperture lead to mass transfer by advective paths that connect the eddy to the main flow channel. This mixing process leads to shortening of BTC tails at higher flow rates The experimental and numerical results imply that the tailing grows strong with increasing fluid velocity, reaching its peak when eddies are about to form, but when eddies become fully developed, the tails, decrease in length, which is contrary to results from previous 2-D computational studies.

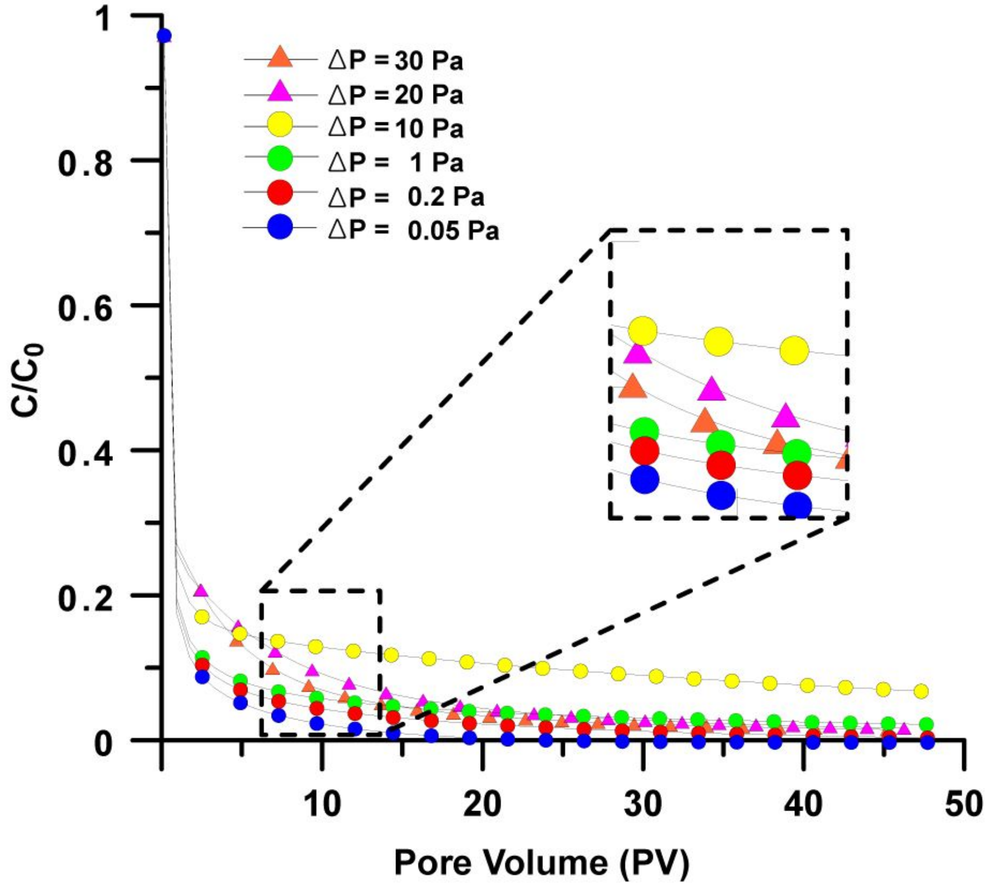

Figure 3-23 The residual concentration of solutes in the large aperture area with PV. The BTCs show that tails reach the highest at ΔP = 10 Pa, but after that, tails turn shortened at ΔP = 20 and 30 Pa.

3.4 Conclusions

We present the first direct observation of fluid flow and solute transport in a microscopic rough-walled fracture using micro-PIV to assess the evolution of non-Fickian tailing as eddies developed at larger fluid velocities. These direct observations of solute transport in a rough-walled fracture demonstrated a previously unidentified, important phenomenon: normalized BTCs became highly skewed toward later times up until a limiting fluid velocity, beyond which tailing decreased and peak concentrations increased. Further microscopic observation of particle trajectories clarified the likely cause of the reduced tailing at higher velocities. Tailing increased until the onset of eddies in large-aperture regions. As eddies became fully developed, particles were initially entrained in the eddies, but then cast back into the main flow channel, which reduced tailing.

To more clearly understand the 3-D nature of the flow and transport, numerical studies were carried out, which showed that the flow trajectory swirled near the fracture walls in a large-aperture region and turned back in the main flow channel, supporting the experimental observation. This study, based on combined direct observations and numerical simulations, clearly demonstrated that there was no well-defined separation stream surface delineating the so-called immobile (recirculation) and mobile zones in the 3-

D nature of the flow and transport and the tails decreased with growing eddies due to mass transfer by advective paths from the inside eddies to the main flow channels. These experimental and numerical results contradict results from numerous previous studies based upon simulations in 2-D fracture geometries and highlight the need for caution when using 2-D simulations to understand 3-D transport processes.

CHAPTER 4.

IMPLICATIONS & FURTHER STUDY

CHAPTER 4. IMPLICATIONS & FURTHER STUDY

4.1 Implications

Our research demonstrates the generation of an eddy flow and its effect on the tail shortening concept via a microscopic approach. The visualized phenomenon was somewhat conceptual, and there remains a limitation with regard to its direct application in field scale experiments. In the future, an improved design of the experiment needs to be developed for linking with field-scale experiments. If the conceptual flow can be confirmed in the field, it would have a wide range of implications with reference to various subjects associated with hydrogeology.

First, the tail shortening mechanism is useful for developing an in-situ remediation scheme. By setting an appropriate groundwater velocity, the remediation efficiency can be increased. On the field scale, a rapid groundwater gradient can be generated by artificial pumping, and the flow velocity range which can occur in a fracture is similar to the range in our experiment. Thus, the eddy and tail shortening concept may be applicable to in-situ remediation techniques such as pump and treat or surfactant flushing. Contaminants near the fracture wall can be efficiently removed by implementing a proper pumping rate to generate an eddy flow.

Secondly, the present results are also applicable to the area of geothermal energy utilization, such as the extraction of heat from hot dry rock (HDR) or the operation of an open-loop geothermal energy system. For geothermal energy, hot water is extracted from a well, and cool water is reinjected through a separated well after utilizing the energy. In this case, regional groundwater velocity is likely to reach 1 m/s while operating the recirculating flow. Thermal dispersion occurs by groundwater advection, which is similar to the solute dispersion mechanism. Hence, an eddy flow and tail shortening concept can be applicable in this case.

In a karst aquifer, medium consisting of limestone and dolomite are soluble, creating considerable degree of heterogeneity in the aquifer and regional fast flows. The flow velocity reaches the turbulent flow regime in nature, which affects the rapid migration of contaminants. Therefore, the transport mechanism in our research can be applied to groundwater transport associated with a karst aquifer.

Lastly, the eddy flow effect may have implications for those who study magma flows. At the upper level of brittle crust, magma flows through discrete fractures. The magma flow regime (i.e., laminar or turbulent) can influence the composition mixing, the heat transfer, and the mass transfer.

4.2 Further study

The Reynolds number in our experiment is limited to 17.1. Although the experiments include a wide range of groundwater flow velocity conditions (See Figure 1-2), they do not include the turbulent flow regime. In the future, the Reynolds number in experiments can be extended to the range of 1000 ~ 2000, by improving the experimental devices (e.g., a high speed CCD camera, a high resolution microscope, and light sources). An earlier experiment by the authors includes the laminar flow and the non-linear laminar flow (weak or strong inertia) regimes. However, previously noted, in case such as a karstic aquifer, in flows during geothermal energy utilization, and during hydraulic fracturing, the fracture flow velocity is likely to reach 1 m/s, which is clearly in the turbulent flow regime. Therefore, an extended experiment including the turbulent flow regime would be meaningful for characterizing various solute transport schemes ranging from the laminar to the turbulent schemes.

Our study was limited to conceptual 3D modeling and to the conceptual visualization of a pore scale flow. Although we present meaningful results for the solute transport mechanism, the results were not proved by directly linked in-situ solute transport experiments. The conceptual findings need to be specified in conjunction with in-situ field fracture experiments. Further, in-situ experiment data from a well to well pumping test or a tracer test can be analyzed through a constructed micromodel representing in-situ pore geometry.

Besides fracture flows, various situations of hydraulic flows can be visualized by taking advantage of micromodels. In previous research on a subject related to colloid transport, DNAPL remediation visualization, the flow characteristics in a double porous medium, and bio-clogging were investigated through a micromodel visualization technique. In the future, it will be necessary to design micromodels to represent various hydraulic flows so as to reveal the mechanisms associated with groundwater flows.

CONCLUDING REMARKS

CONCLUDING REMARKS

This study focuses on the characterization of fluid flow and solute transport in a highly rough-walled fracture with visualization techniques. Understanding the flow and the transport in a fractured rock medium located tens to hundreds of meters below the surface is a challenging issue in hydrogeology. Due to the limited pore scale geometry information, it is very difficult to reveal the detailed transport mechanism with regards to fracture geometry. In this case, to understanding flow and transport in pore-scale, micro-scale approaches based on constructed micro-models provide a solid interpretation of the phenomena in field scale.

The roughness conditions of the single fracture were duplicated for the experiment, and then an acrylic single rough-walled fracture called the micromodel was constructed. Through the experiment with the micromodel and microscope, a direct visualization of the hydraulic flow in a pore-scale was achieved. Although the single-phase flows were visualized in my studies, a visualization through the micromodel can be widely utilized to determine various phenomena under more complex flow conditions in hydrogeology (e.g. pore scale flow visualization, multi-phase interaction in the pore scale, investigating hysteresis in a saturated-unsaturated condition, interactions in double porous medium, and calculating the partitioning coefficient contact area between two immiscible phases).

An observation through a micromodel has obvious limitations in that the duplicated porous medium is not real rock material, but there are clear advantages. For example, fluid flow can be observed by the naked eye with an artificially constructed micromodel. The results of tracer tests under in-situ conditions do not provide an interpretation from pore scale effects. In the case, research associated with flow visualization in microscopic approaches gives insight to the field scale phenomena which is difficult to prove under in-situ conditions.

In this research, micro particle image velocimetry (PIV) technique was applied to determine the velocity vectors in a constructed single rough-walled fracture model. The velocity distributions are utilized to assess the validity of the Stokes and the Reynolds equations, which are the simplified forms of the Navier - Stokes equations. The study first attempted to utilize the microPIV to investigate the surface roughness of fracture wall on fluid flow. The MicroPIV technique is a powerful tool in understanding the fluid flow characteristics under various pore-scale geometry conditions.

In addition, 2-D and 3-D numerical N-S flow simulations were carried out to support the experimentally observed phenomena. According to previous studies, the tailing effects of breakthrough curves occurred due to the growth of the recirculation zones under high velocity conditions. However, the previous studies are limited to 2-D N-S flow simulations. Our 2-D and 3-D numerical simulation results with experimentally visualized images showed that the tail shortening of breakthrough curves (BTCs) occurred from eddy flow, which is a noteworthy discovery. The concept of tail-shortening in a rough-walled fracture under high velocity conditions will be useful for interpreting solute transport in the fractured medium.

References

Auradou, H. (2009), Influence of wall roughness on the geometrical, mechanical and transport properties of single fractures, J. Phys. D: Appl. Phys., 42(21), doi:10.1088/0022-3727/42/21/214015.

Becker, M. W. and A. M. Shapiro (2000), Tracer transport in fractured crystalline rock: Evidence of nondiffusive breakthrough tailing, *Water Resour. Res., 36,* 1677-1686, doi:10.1029/2000WR900080.

Berkowitz, B. (2002), Characterizing flow and transport in fractured geological media: A review, *Adv. Water. Resour.,* 25, 861-884.

Blessent, D., R. Therrien, and C. W. Gable (2011), Large-scale numerical simulation of groundwater flow and solute transport in discretely-fractured crystalline bedrock, *Adv. Water. Resour.*, 34(12), 1539-1552, doi:10.1016/j.advwatres.2011.09.008.

Bigi, S., M. Battaglia, A. Alemanni, S. Lombardi and A. Campana (2013), CO_2 flow through a fractured rock volume: Insights from field data, 3D fractures representation and fluid flow modeling, *Int. J. Greenh. Gas Con.,* 18, 183-199.

Bodin, J., F. Delay, and G. De Marsily (2003a), Solute transport in a single fracture with negligible matrix permeability: 1. fundamental mechanisms, *Hydrogeol. J.,* 11(4), 418-433, doi:10.1007/s10040-003-0268-2.

Bodin, J., F. Delay, and G. De Marsily (2003b), Solute transport in a single fracture with negligible matrix permeability: 2. mathematical formalism, *Hydrogeol. J.*, 11(4), 434-454,doi:10.1007/s10040-003-

0269-1.

Bolster, D., M. Dentz, and T. Le Borgne (2009), Solute dispersion in channels with periodically varying apertures, *Phys. Fluids*, 21, 056601, doi:10.1063/1.3131982.

Bolster, D., Y. Meheust, T. Le Borgne, J.Bouquain, and P. Davy (2014), Modeling preasymtotic transport in flow with significant inertial and trapping effects – The importance of velocity correlations and a spatial Markov model, *Adv. Water Resour., 70,* 89-103, doi:10.1016/advwatres.2014.04.014.

Borgne, T., O. Bour, F. L. Paillet and J.-P. Caudal (2006), Assessment of preferential flow path connectivity and hydraulic properties at single-borehole and cross-borehole scales in a fractured aquifer, *J.Hydrol.,* 328, 347-359.

Boschan, A., I. Ippolito, R. Chertcoff, H. Auradou, L. Talon, and J. Hulin (2008), Geometrical and Taylor dispersion in a fracture with random obstacles: An experimental study with fluids of different rheologies, *Water Resour. Res.*, 44(6), W06420, doi:10.1029/2007WR006403.

Bouquain, J., Y. Meheust, D. Bolster, and P. Davy (2012), The impact of inertial effects on solute dispersion in a channel with periodically varying aperture, *Phys. Fluids*, 24(8), doi:10.1063/1.4747458.

Boutt, D. F., G. Grasselli, J. T. Fredrich, B. K. Cook, and J. R. Williams (2006), Trapping zones: The effect of fracture roughness on the directional anisotropy of fluid flow and colloid transport in a single fracture, *Geophys. Res. Lett.*, 33, L21402, doi:10.1029/2006GL027275.

Brown, S. R. (1987), Fluid flow through rock joints: The effect of surface roughness, *J. Geophys. Res.*, 92(B2), 1337–1347, doi:10.1029/JB092iB02p01337.

Brush, D. J., and N. R. Thomson (2003), Fluid flow in synthetic rough-walled fractures: Navier-Stokes, Stokes, and local cubic law simulations, *Water Resour. Res.,* 39(4), 1085. doi:10.1029/2002WR001346.

Cardenas, M. B., D. T. Slottke, R. A. Ketcham, and J. M. Sharp (2007), Navier-Stokes flow and transport simulations using real fractures shows heavy tailing due to eddies, *Geophys. Res. Lett.,* 34(14), L14404, doi:10.1029/2007GL030545.

Cardenas, M. B., D. T. Slottke, R. A. Ketcham, and J. M. Sharp Jr. (2009), Effects of inertia and directionality on flow and transport in a rough asymmetric fracture, *J. Geophys. Res.,* 114, B06204, doi:10.1029/2009JB006336.

Carneiro, J. F. (2009), Numerical simulations on the influence of matrix diffusion to carbon sequestration in double porosity fissured aquifers, *Int. J. Greenh. Gas. Con.,* 3(4), 431-443. doi:10,1016/j.ijggc.2009.02.006.

COMSOL AB (2013), COMSOL Multiphysics Reference Manual version 4.4, Stockholm.

Chaudhary, K., M. B. Cardenas, W. Deng, and P. C. Bennett (2011), The role of eddies inside pores in the transition from Darcy to Forchheimer flows, *Geophys. Res. Lett.,* 38, L24405, doi:10.1029/2011GL050214.

Chaudhary, K., M. B. Cardenas, W. Deng, and P. C. Bennett (2013), Pore geometry effects on intrapore viscous to inertial flows and on effective hydraulic parameters, *Water Resour. Res.,* 49, doi:10.1002/wrcr.20099

Detwiler, R. L., H. Rajaram, and R. J. Glass (2000), Solute transport in variable-aperture fractures: An investigation of the relative importance of Taylor dispersion and macrodispersion, *Water Resour. Res.*, 36(7), 1611-1625.

Dietrich, P., Helmig, R., Sauter, M., Hötzl, H., Köngeter, J., and G. Teutsch (Eds.). (2005), *Flow and transport in fractured porous media*. Springer Science & Business Media.

Dronfield, D. G., and S. E. Silliman (1993), Velocity dependence of dispersion for transport through a single fracture of variable roughness, *Water Resour. Res.*, 29(10), 3477-3483.

Ge, S. (1997), A governing equation for fluid flow in rough fractures, *Water Resour. Res.*, 33(1), 53–61, doi:10.1029/96WR02588.

Giacomini, A., O. Buzzi, A. Ferrero, M. Migliazza, and G. Giani (2008), Numerical study of flow anisotropy within a single natural rock joint, *Int. J. Rock Mech. Min. Sci.*, 45(1), 47-58, doi:10.1016/j.ijrmms.2007.04.007.

Hakami, E., and E. Larsson (1996), Aperture measurements and flow experiments on a single natural fracture, *Int. J. Rock Mech. Min. Sci. Geomech. Abstr.,* 33(4), 395-404 doi:10.1016/0148-9062(95)00070-4

Huber, F., F. Enzmann, A. Wenka, M. Bouby, M. Dentz, and T. Schäfer (2012), Natural micro-scale heterogeneity induced solute and nanoparticle retardation in fractured crystalline rock, *J. Contam. Hydrol.,* 133(15), 40-52, doi:10.1016/j.jconhyd,2012.03.004.

Ippolito, I., G. Daccord, E. Hinch, and J. Hulin (1994), Echo tracer dispersion in model fractures with a rectangular geometry, *J. Contam. Hydrol.,* 16(1), 87-108, doi:10.1016/0169-7722(94)90073-6.

Ishibashi, T., Watanabe, N., Hirano, N., Okamoto, A., and N. Tsuchiya (2012). GeoFlow: A novel model simulator for prediction of the 3-D channeling flow in a rock fracture network. *Water Resour. Res.*, *48*(7), doi:10.1029/2011WR011226.

Karpyn, Z. T., A. Alajmi, F. Fadaelli. P. M. Halleck, and A. S. Grader (2009). X-ray CT and hydraulic evidence for a relationship between fracture conductivity and adjacent matrix porosity, *Eng. Geol., 103(*3-4), 139-145, doi:10.1016/j.enggeo.2008.06.017.

Keller, A. A. (1998), High resolution, non-destructive measurement and characterization of fracture apertures, *Int. J. Rock. Mech. Min. Sci, 35*(8), 1037-1050, doi:10.1016/S0148-9062(98)00164-8.

Keller, A. A., P. V. Roberts, and P. K. Kitanidis (1995), Prediction of single phase transport parameters in a variable aperture fracture, *Geophys.*

Res. Lett., 22(11), 1425-1428, doi:10. 1029/95GL01497.

Keller, A. A., P. V. Roberts, and M. J. Blunt (1999), Effect of fracture aperture variations on the dispersion of contaminants, *Water Resour. Res.*, 35(1), 55-63, doi:10. 1029/1998WR900041.

Konzuk, J. S., and B. H. Kueper (2004), Evaluation of cubic law based models describing single-phase flow through a rough-walled fracture, *Water Resour. Res.*, 40(2), W02402, doi:10.1029/2003WR002356.

Koyama, T., I. Neretnieks, L. Jing (2008), A numerical study on differences in using Navier-Stokes and Reynolds equations for modeling the fluid flow and particle transport in single rock fractures with shear, *Int. J. Rock. Mech. Min. Sci.*, 45(7), 1082-1101, doi:10.1016/j.ijrmms.2007.11.006.

Kreft, A., and A. Zuber (1978), On the physical meaning of the dispersion equation and its solutions for different initial and boundary conditions, *Chem. Eng. Sci., 33,* 1471-1480.

Lakowicz, J. R. (2006), *Principles of Fluoresence Spectroscopy,* Springer, New York.

Lapcevic, P. A., K. S. Novakowski, and E. A. Sudicky (1999), The interpretation of a tracer experiment conducted in a single fracture under conditions of natural groundwater flow, *Water Resour. Res., 35*(8), 2301-2312, doi:10.1029/1999WR900143.

Lee, H. B., Yeo, I. W., and K. K. Lee (2007). Water flow and slip on NAPL-wetted surfaces of a parallel-walled fracture. *Geophys. Res.*

Lett., *34*(19).

Lee, H.-B., Yeo, I. W., Ji, S. -H. and K.-K. Lee (2010), Wettability-dependent DNAPL migration in a rough-walled fracture, *J. Contam. Hydrol., 113,* 44-55, doi:10.1016/j.jconhyd.2009.12.006.

Leij, F. J., and J. H. Dane (1991). Solute transport in a two-layer medium investigated with time moments, *Soil Sci. Soc. Am. J., 55,* 1529-1535.

Lee, S. H., K.-K. Lee, and I. W. Yeo (2014), Assessment of the validity of Stokes and Reynolds equations for fluid flow through a rough-walled fracture with flow imaging, *Geophys. Res. Lett., 41,* 4578-4585, doi:10.1002/2014GL060481.

Li, H., and M. Olsen (2006), MicroPIV measurements of turbulent flow in square microchannels with hydraulic diameters from 200 μm to 640 μm, *Int. J. Heat Fluid Fl.*, 27(1), 123-134, doi:10.1016/j.ijheatfluidflow.2005.02.003.

Mallikamas, W., and H. Rajaram (2010), An improved two-dimensional depth-integrated flow equation for rough-walled fractures, *Water Resour. Res.*, 46, W08506, doi:10.1029/2009WR008779.

McLaren, R. G., E. A. Sudicky, Y.-J. Park, and W. A. Illman (2012), Numerical simulation of DNAPL emissions and remediation in a fractured dolomitic aquifer, *J. Contam. Hydrol.,* 136–137, 56-71, doi:10.1016/j.jconhyd.2012.05.002.

Moreno, L., I. Neretnieks, and T. Eriksen (1985), Analysis of some laboratory tracer runs in natural fissures, *Water Resour. Res., 21*(7), 951-958, doi:10.1029/WR021i007p00951.

Myers, T. (2012), Potential contaminant pathways from hydraulically fractured shale to aquifers, *Groundwater,* 50, 6, 872-882.

Neretnieks, I. (1983), A note on fracture flow dispersion mechanism in the ground, *Water Resour. Res., 19*(2), 364-370, doi: 10.1029/WR019i002p00364.

Neretnieks, I., T. Eriksen, and P. Tähtinen (1982), Tracer movement in a single fissure in granitic rock: Some experimental results and their interpretation, *Water Resour. Res., 18*(4), 849-858, doi:10.1029/WR018i004p00849.

Novakowski, K., P. A. Lapcevic, J. Voralek, and G. Bickerton (1995), Preliminary interpretation of tracer experiments conducted in a discrete rock fracture under conditions of natural flow, *Geophys. Res. Lett., 22,* 1417-1420, doi:10.1029/95GL00569.

Nicholl, M. J., H. Rajaram, R. J. Glass, and R. Detwiler (1999), Saturated flow in a single fracture: evaluation of the Reynolds Equation in measured aperture fields, *Water. Resour. Res.*, 35(11), 3361–3373, doi:10.1029/1999WR900241.

Oron, A. P. and B. Berkowitz (1998), Flow in rock fractures: The local cubic law assumption reexamined, *Water Resour. Res.*, 34(11), 2811–2825, doi:10.1029/98WR02285.

Potter, C. J., W. C. Day, D. S. Sweetkind and R. P. Dickerson (2004), Structural geology of the proposed site area for a high-level radioactive waste repository, Yucca Mountain, Nevada, *Geol. Soc. Am. Bull.,*116, 7/8, 858-879.

Qian J., Z. Chen, H. Zhan, and H. Huan (2011), Experimental study of the effect of roughness and Reynolds number on fluid flow in rough-walled single fractures: a check of local cubic law, *Hydrol. Process*., 25, 614-622, doi:10.1002/hyp.7849.

Qian, J., M. Liang, Z. Chen, and H.Zhan (2012), Eddy correlations for water flow in a single fracture with abruptly changing aperture, *Hydrol. Process., 26,* 3369-3377, doi:10.1002/hyp.8332.

Rasouli, V., and A. Hosseinian (2011), Correlations developed for estimation of hydraulic parameters of rough fractures through the simulation of JRC flow channels, *Rock Mech. Rock Eng.*, 44, 447-461, doi:10.1007/s00603-011-0148-3.

Raven, K. G., K. S. Novakowski, and P. A. Lapcevic (1988), Interpretation of field tracer tests of a single fracture using a transient solute storage model, *Water Resour. Res., 24*(12), 2019-2032, doi:10.1029/WR024i012p02019.

Reeves, D. M., D. A. Benson, *and* M. M. Meerschaert (2008), Influence of fracture statistics on advective transport and implications for geologic repositories, *Water Resour. Res.*, 44, *W08405, doi:*10.1029/2007WR006179.

Renshaw, C. E., J. S. Dadakis, and S. R. Brown (2000), Measuring fracture apertures: A comparison of methods, *Geophys. Res. Lett.*, 27(2), 289–292, doi:10.1029/1999GL008384.

Roux, S., F. Plouraboué, and J. P. Hulin (1998), Tracer dispersion in rough open cracks, *Transp. Porous Med.*, 32(1), 97-116, doi:10.1023/A:1006553902753.

Tongwa, P., R. Nygaard, A. Blue and B. Bai (2013), Evaluation of potential fracture-sealing materials for remediating CO_2 leakage pathways during CO_2 sequestration, *Int. J. Greenh. Gas Con.,* 18, 128-138.

Tsang, Y. W., and C. F. Tsang (1987), Channel model of flow through fractured media, *Water Resour. Res., 23*(3), 467-479, doi:10.1029/WR023i003p00467.

White, F. M. (2011), *Fluid Mechanics,* McGraw-Hill, New York.

Yeo, I. W., M. H. de Freitas, and R.W. Zimmerman (1998), Effect of shear displacement on the aperture and permeability of a rock fracture, *Int. J. Rock Mech. Min. Sci.*, 35(8), 1051-1070, doi:10.1016/S0148-9062(98)00165-X.

Yeo, W. (2001), Effect of fracture roughness on solute transport, *Geosci. J.,* 5(2), 145-151, doi:10.1007/BF02910419.

Yu, C., A. W. Warrick, and M. H. Conkline (1999), A moment method for analyzing breakthrough curves of step inputs, *Water Resour. Res., 35*(11), 3567-3572.

Zheng, X., and Z. Silber-Li (2008), Measurement of velocity profiles in a rectangular microchannel with aspect ratio $\alpha = 0.35$, *Exp. Fluids,* 44(6), 951-959, doi: 10.1007/s00348-007-0454-4.

Zhou, Q., H.-H. Liu, G. S. Bodvarsson, and F. J. Molz (2006), Evidence of multi-process matrix diffusion in a single fracture from a field tracer test, *Transport Porous Media, 63,* 473-487, doi:10.1007/s11242-005-1123-9.

Zimmerman, R. W., and G. S. Bodvarsson (1996), Hydraulic conductivity of rock fractures, *Transp. Porous Med.*, 23(1), 1-30, doi: 10.1007/BF00145263.

Zimmerman, R. W., and I. W. Yeo (2000), Fluid flow in rock fractures: From the Navier-Stokes equations to the cubic law, in *Dynamics of Fluids in Fractured Rock*, *Geophys. Monogr. Ser.*, 122, 213–224, doi:10.1029/GM122p0213.

Zimmerman, R. W., A. Al-Yaarubi, C. C. Pain, and C. A. Grattoni (2004), Non-linear regimes of fluid flow in rock fractures, *Int. J. Rock Mech. Min. Sci.*, 41(3), 163-169,doi:10.1016/j.ijrmms.2004.03.036.

Zou, L., Jing, L., and V. Cvetkovic (2015). Roughness decomposition and nonlinear fluid flow in a single rock fracture. *Int. J. Rock Mech. Min. Sci.*, *75*, 102-118.

국문 초록

거친 표면을 가진 단열대에서 유체의 유동과 용질의 거동을 이해하는 것은 석유 저장층의 개발, 지열 발전, 이산화탄소 지중 저장층 및 방사성 폐기물 심지층 처리의 안정성 평가 등의 문제를 다룰 때 매우 중요하다.

본 연구에서는 단열에서의 유체의 흐름을 이해하기 위하여 거친 단일 절리조건에서 레이놀즈 수 0.014에서 0.086 범위에서 microPIV 기법을 이용하여 단열 내 속도 분포를 측정하였다. 측정된 속도 분포자료를 이용하여 나비에 스토크스 방정식의 간단화된 형식인 스토크스 방정식과 레이놀즈 방정식의 가정들의 정당성을 평가하기 위해서 나비에 스토크스 방정식의 각 항의 크기를 비교하는 연구를 수행하였다. 그 결과, 굉장히 거칠기가 큰 지역이라도 점성력 항은 관성력 항보다 2 order 이상 더 큰 크기를 가졌으며, 이를 통해 나비에 스토크스 방정식에서 관성력 항을 제외시킨 스토크스 방정식이 레이놀즈 수 0.1 이하의 범위에서 활용 가능하다고 판단하였다. 하지만, 스토크스 방정식에서 레이놀즈 방정식으로 간단화 시킬 때는 $\partial^2 u_x / \partial z^2$ 항이 다른 점성력 항보다 매우 커야 하지만, 속도 분포자료를 이용한 해석 결과 레이놀즈 수 0.1 이하 범위의 거칠기가 큰 단열 흐름에서 이 가정은 맞지 않는 것으로 나타났으며, 이는 레이놀즈 방정식은 실제 유량의 흐름을 과대평가할 우려가 있다는 것을 의미한다.

또한, 거친 단열의 표면에서의 와류의 형성이 단열 내 용질의 거동에 미치는 영향을 평가하기 위해서, 현미경을 이용한 미시적인 용질거동의 관찰을 수행하였다. 그 결과, 거칠기가 큰 단열

공극에서 속도 증가에 따른 와류의 형성 및 성장이 관찰되었다. 유체에 희석된 형광입자는 와류에 포획되어 회전하다가 다시 주 흐름 경로로 돌아가는 형태를 보이는데 이는 용질이력곡선에서의 tailing 현상을 감소시키는 역할을 하는 것이 발견되었다. 이는 기존의 용질거동개념모델에서 알려진 유동구역과 비유동구역이 구분된 흐름이 형성되어 두 유역간은 상호작용을 하지 않는다는 일치하지 않는 내용이다. 또한, 본 연구에서 수행된 3-D 개념모델에서의 유체유동과 용질거동 수치모델링 결과, 실험에서 관찰된 테일링(tailing) 현상의 감소는 두 구역간의 용질 전달이 확산 기작이 아닌 와류에 의한 이송 기작으로의 전달이 이루어 진다는 것을 확인하였다. 이는 기존의 2-D 수치모델링 연구들에서 속도증가에 따라 와류의 크기가 증가함에 따라 테일링(tailing)이 길어진다는 연구에 대한 상반된 연구내용으로 2-D 수치모델링을 통해 실제 단열대의 유동을 해석할 때 전혀 다른 결과를 가져올 수 있으므로 유의해야 할 것 이다.

주요어: 마이크로입자영상유속계, 용질거동이력곡선, 거친 단열, 와류, 나비에 스토크스 방정식, 레이놀즈 방정식, 테일링 현상